Molecular architecture determines brain delivery of a transferrin receptor–targeted lysosomal enzyme

Annie Arguello[1]* , Cathal S. Mahon[1]* , Meredith E.K. Calvert[1] , Darren Chan[1] , Jason C. Dugas[1] , Michelle E. Pizzo[1] , Elliot R. Thomsen[1] , Roni Chau[1] , Lorna A. Damo[1] , Joseph Duque[1] , Meng Fang[1] , Tina Giese[1] , Do Jin Kim[1] , Nicholas Liang[1] , Hoang N. Nguyen[1] , Hilda Solanoy[1] , Buyankhishig Tsogtbaatar[1] , Julie C. Ullman[1] , Junhua Wang[1] , Mark S. Dennis[1] , Dolores Diaz[1] , Kannan Gunasekaran[1] , Kirk R. Henne[1] , Joseph W. Lewcock[1] , Pascal E. Sanchez[1] , Matthew D. Troyer[1] , Jeffrey M. Harris[1] , Kimberly Scearce-Levie[1] , Lu Shan[1] , Ryan J. Watts[1] , Robert G. Thorne[1,2] , Anastasia G. Henry[1] , and Mihalis S. Kariolis[1]

Delivery of biotherapeutics across the blood–brain barrier (BBB) is a challenge. Many approaches fuse biotherapeutics to platforms that bind the transferrin receptor (TfR), a brain endothelial cell target, to facilitate receptor-mediated transcytosis across the BBB. Here, we characterized the pharmacological behavior of two distinct TfR-targeted platforms fused to iduronate 2-sulfatase (IDS), a lysosomal enzyme deficient in mucopolysaccharidosis type II (MPS II), and compared the relative brain exposures and functional activities of both approaches in mouse models. IDS fused to a moderate-affinity, monovalent TfR-binding enzyme transport vehicle (ETV:IDS) resulted in widespread brain exposure, internalization by parenchymal cells, and significant substrate reduction in the CNS of an MPS II mouse model. In contrast, IDS fused to a standard high-affinity bivalent antibody (IgG:IDS) resulted in lower brain uptake, limited biodistribution beyond brain endothelial cells, and reduced brain substrate reduction. These results highlight important features likely to impact the clinical development of TfR-targeting platforms in MPS II and potentially other CNS diseases.

Introduction

The use of protein-based therapies to treat neurodegenerative diseases has been limited by minimal brain exposure following systemic administration (Kumar et al., 2018; Stanimirovic et al., 2018). Most polar small molecules and nearly all macromolecules are effectively restricted from reaching the brain in therapeutically relevant concentrations by physical and biochemical barriers, most notably the blood–brain barrier (BBB; Abbott et al., 2018; Banks, 2016). Brain endothelial cells that form the BBB have several unique physiological properties that distinguish them from peripheral endothelial cells, including tight junctions, relatively low endocytic activity, and the expression of numerous transporters and receptors (Profaci et al., 2020). As a result, central nervous system (CNS) concentrations of antibodies often reach only about 0.01–0.1% (Atwal et al., 2011; Poduslo et al., 1994; St-Amour et al., 2013) of peripheral levels after systemic administration, and typically, much of the brain-associated antibody is confined to the endothelium and not parenchymal cells (St-Amour et al., 2013).

A promising strategy to improve brain uptake of biotherapeutics leverages receptor-mediated transcytosis (RMT) at the BBB (Banks, 2016; Lajoie and Shusta, 2015). RMT is an endogenous process wherein essential biomolecules that cannot passively diffuse into the brain from the bloodstream are actively transported across brain endothelial cells via specific receptors on their luminal surface (Johnsen et al., 2019). Whereas some brain endothelial cell receptors capable of initiating RMT are downregulated postnatally (e.g., mannose-6-phosphate receptor [M6PR]; Urayama et al., 2004; Urayama et al., 2008), other receptors capable of RMT such as the transferrin receptor (TfR) are expressed throughout life (Preston et al., 2014). Biotherapeutic platforms engineered to interact with persistently expressed receptors can therefore exploit RMT pathways to gain access to the CNS (Johnsen et al., 2019; Jones and Shusta, 2007).

TfR has been among the most studied RMT targets at the BBB (Johnsen et al., 2019), owing in part to its enriched expression on brain endothelial cells (Jefferies et al., 1984) and its constitutive ligand-independent endocytosis (Hopkins et al., 1985). Many platforms targeting TfR have been described (Terstappen et al., 2021), including conventional high-affinity bivalent antibodies (Friden et al., 1991), bispecific antibodies (Yu et al., 2011), antibody fragments (Lesley et al., 1989), peptides (Kuang et al., 2016), antibody-fusion architectures (Hultqvist et al., 2017;

Niewoehner et al., 2014; Sonoda et al., 2018), and most recently, a transport vehicle (TV) consisting of an Fc domain engineered to directly bind TfR (Kariolis et al., 2020). Of these, traditional antibodies directed against target receptors have several attractive features, most notably, established discovery and development methods to generate specificity and high affinity. Several antibodies have been reported that engage TfR bivalently with subnanomolar apparent affinities (Pardridge, 2015; Sonoda et al., 2018). While such antibodies are capable of being internalized into brain endothelial cells, a number of imaging and biodistribution studies in mouse models have suggested they may be only minimally released into the brain parenchyma (Moos and Morgan, 1998; Paris-Robidas et al., 2011; Paterson and Webster, 2016; Yu et al., 2011). Studies using monovalent anti-TfR antibodies with weaker affinity have shown enhanced BBB transcytosis and brain accumulation (Bien-Ly et al., 2014; Weber et al., 2018; Yu et al., 2011). A proposed mechanism for the increased brain uptake is altered intracellular trafficking, whereby weaker affinity anti-TfR antibodies avoid sorting to lysosomes and subsequent degradation, while high-affinity anti-TfR antibodies mainly accumulate in lysosomes driving receptor degradation (Bien-Ly et al., 2014). Several studies have demonstrated that the intrinsic properties of TfR-directed architectures (including affinity and valency) can impact transport across the BBB (Dennis and Watts, 2012; Moos and Morgan, 2001; Villasenor et al., 2019; Villasenor et al., 2017; Yu et al., 2011). Despite these studies, questions around the most suitable TfR-targeting molecular architecture for optimal brain delivery have remained. This is particularly relevant for lysosomal storage disorders (LSDs), for which traditional high-affinity, bivalent TfR-binding antibody fusions and newer monovalent TfR-binding TV-fusions are currently being evaluated in the clinic (NCT04251026, 2022; Okuyama et al., 2019; Okuyama et al., 2021).

The primary treatment for LSDs involves enzyme replacement therapies (ERTs) that have limited transport across the BBB and therefore represent an attractive candidate cargo to examine the relative merits of specific TfR-based approaches. LSDs represent a family of >50 monogenic diseases, many of which are characterized by a defect in a single lysosomal enzyme (Neufeld, 1991; Schultz et al., 2011). Disease-associated variants lead to a reduction or loss of enzymatic activity, resulting in substrate accumulation and broad lysosomal dysfunction (Platt et al., 2012). Perturbed lysosomal function can trigger pathogenic cascades affecting multiple tissues throughout the body, including the CNS (Bellettato and Scarpa, 2010). At present, the standard of care for many LSDs is systemically administered recombinant ERTs; however, these enzymes do not readily cross the BBB and typically have been ineffective in treating the CNS manifestations of disease (Desnick and Schuchman, 2012; Muldoon et al., 2013; Scarpa et al., 2015). Mucopolysaccharidosis II (MPS II) is an X-linked LSD resulting from deficient activity of iduronate-2-sulfatase (Schultz et al., 2011), an enzyme responsible for the catabolism of the glycosaminoglycans (GAGs) heparan and dermatan sulfate (Wraith et al., 2008). MPS II is characterized by widespread GAG accumulation with a host of secondary pathologies, and nearly 70% of patients present with neuronopathic disease (Noh and Lee, 2014). Since its approval in 2006, recombinant IDS has transformed the clinical management of MPS II, successfully reducing GAG accumulation in the periphery (Muenzer et al., 2006; Sohn et al., 2013). However, administration of recombinant IDS does not effectively treat CNS pathology (Parini and Deodato, 2020; Scarpa et al., 2017), highlighting the critical need for the development of new brain-penetrant therapies for MPS II.

We recently described a TV-based biotherapeutic for MPS II generated by fusing IDS to an engineered TfR-binding Fc fragment (ETV:IDS; Kariolis et al., 2020; Ullman et al., 2020). ETV: IDS binds TfR monovalently with a moderate affinity identified to maximize brain uptake, in contrast to most other TfR-based enzyme platforms in which enzymes have been fused to high-affinity, bivalent anti-TfR antibodies (Boado et al., 2018; Sonoda et al., 2018; Zhou et al., 2012). Importantly, the monovalent, moderate TfR affinity and bivalent, high TfR affinity approaches are each being evaluated as new IDS ERTs with the potential for CNS efficacy in ongoing and planned multicenter clinical trials in the United States for MPS II (NCT04251026; NCT04573023). Characterizing how these different molecular architectures impact CNS biodistribution and potency preclinically therefore has significant relevance for their clinical translation.

Here, we compare ETV:IDS to a high-affinity, bivalent TfR-binding antibody-enzyme fusion with IDS (IgG:IDS) to determine which of these formats currently under clinical investigation most effectively enables broad biodistribution of IDS to the brain following systemic administration. Biodistribution was quantitatively assessed using a combination of bulk tissue measurements, tissue fractionation, fluorescence imaging, and superresolution confocal microscopy (SRCM). Activity was evaluated by measurements of total GAG levels in liver, brain, and cerebrospinal fluid (CSF) in a mouse model of MPS II. We demonstrated that ETV:IDS results in enhanced brain exposure compared with IgG:IDS. Importantly, ETV:IDS reduced brain and CSF GAG levels to a greater extent than IgG:IDS, likely as a direct reflection of improved biodistribution.

Results and discussion

Biochemical characterization of ETV:IDS and IgG:IDS demonstrates impact of architecture on receptor affinity

ETV:IDS was engineered by fusing IDS to the N-terminus of the TV, as previously described (Ullman et al., 2020), and IgG:IDS was generated by fusing IDS to the C-terminus of both heavy chains of a high-affinity, anti-TfR antibody, similar to a prior description (Sonoda et al., 2018; Fig. 1 A). Additionally, IgG:IDS contains a wild-type Fc domain with preservation of FcγR binding (i.e., full effector function), whereas ETV:IDS has mutations in the Fc to attenuate effector function (Ullman et al., 2020). IDS requires several posttranslational modifications for proper biological function (Demydchuk et al., 2017; Millat et al., 1997) that can be altered by the expression and purification processes. To distinguish parameters created by process (e.g., posttranslational modifications) from properties intrinsic to platform architecture (e.g., affinity and valency), we first characterized the in vitro biochemical enzymatic activity of purified ETV:IDS and IgG:IDS. As ETV:IDS production and
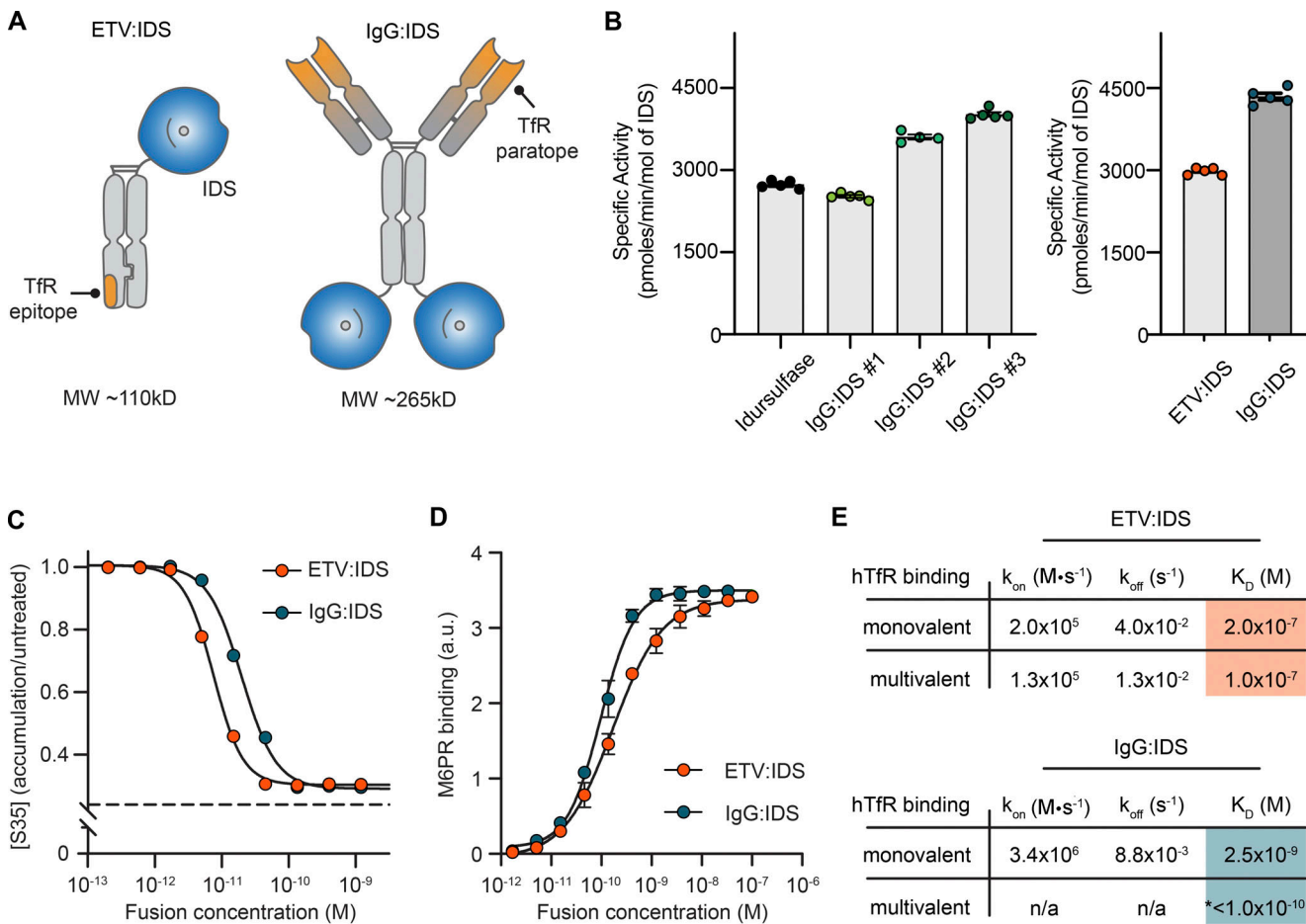
Arguello et al.
Architecture determines brain delivery of enzymes

Journal of Experimental Medicine 2 of 15
https://doi.org/10.1084/jem.20211057

Figure 1. **Biochemical characterization of ETV:IDS and IgG:IDS. (A)** ETV:IDS is a fusion of the lysosomal enzyme IDS to the TV, a TfR-binding Fc domain. IgG:IDS is a high-affinity anti-TfR huIgG fused to IDS at the C-terminus of each heavy chain. **(B)** Specific activities of ETV:IDS and IgG:IDS were measured using a synthetic fluorogenic substrate. Graphs display mean ± SD. Samples represented. Left: Idursulfase (commercially approved recombinant IDS), three IgG:IDS preparations generated by cotransfecting CHO cells with increasing amounts of SUMF1 leading to increasing specific activity. Right: ETV:IDS and high-activity IgG:IDS were chosen for further characterization. **(C)** [^{35}S]sulfate-labeled substrates in MPS II patient-derived fibroblasts after treatment with ETV:IDS or IgG: IDS. n = 3 experiments with three patient lines per phenotype used in each experiment. Dashed line represents the amount of ^{35}S-labeled substrate in healthy control cells. **(D)** Binding affinities of ETV:IDS and IgG:IDS to M6PR were determined by ELISA; n = 3 technical replicates, representative graph shown. **(E)** Monovalent affinities and multivalent apparent affinities of ETV:IDS and IgG:IDS to hTfR were measured by surface plasmon resonance. K_D, equilibrium dissociation constant; k_{off}, dissociation rate constant; k_{on}, association rate constant. *, the value reported for the multivalent interaction between hTfR and IgG: IDS represents an apparent affinity. n/a, the complex binding kinetics for the multivalent IgG:IDS prevented binding kinetics from being fitted. Graph displays mean values across all experimental replicates ± SEM. a.u., arbitrary unit.

associated activities have been previously described (Ullman et al., 2020), we focused here on generating active IgG:IDS. Variations in the expression conditions yielded batches of IgG: IDS with increasing levels of specific activity (benchmarked to idursulfase; Fig. 1 B, left panel, IgG:IDS #1–3). Using optimized conditions, a batch of IgG:IDS that had 1.5-fold higher IDS activity compared with ETV:IDS (Fig. 1 B, right panel) was generated for further characterization as the most stringent comparison against ETV:IDS in biodistribution and efficacy studies.

The activities of ETV:IDS and IgG:IDS were assessed in MPS II patient-derived fibroblasts using an established ^{35}S pulse-chase assay, in which ^{35}S is integrated into newly synthesized GAGs (Lu et al., 2010; Ullman et al., 2020). These fibroblast lines showed significant accumulation of heparan and dermatan sulfate and led to an ~2.5-fold accumulation of ^{35}S signal (Ullman

et al., 2020). Both ETV:IDS and IgG:IDS were highly active in reducing accumulation of ^{35}S-labeled substrates, with cellular median inhibitory concentration (IC$_{50}$) values of 7.5 and 20 pM, respectively (Fig. 1 C). The higher activity of ETV:IDS in a cellular context was surprising given that IgG:IDS was 1.5-fold more active with respect to in vitro specific activity; however, cellular activity represents a complex integration of cell binding and uptake (through TfR and M6PR interactions), delivery to the lysosome, and enzymatic activity within the lysosomal environment. We therefore further characterized the interactions with TfR and M6PR to better understand what might underlie differences in our in vitro and cellular results.

IDS functionality (including biodistribution) is strongly influenced by the incorporation of M6P on the terminal branches of N-linked glycosylations and its ability to bind to M6PR. To confirm that the different architectures retained

strong M6PR binding, the affinities of ETV:IDS and IgG:IDS were determined using ELISA. ETV:IDS bound recombinant M6PR with a median effective concentration (EC_{50}) of 140 pM, whereas IgG:IDS bound with an EC_{50} of 75 pM (Fig. 1 D). The approximately twofold difference in M6PR affinity may reflect multivalent receptor interactions of the two IDS enzymes in IgG:IDS (compared with one in ETV:IDS). As M6PR provides an essential trafficking pathway for targeting enzymes from the extracellular space to the lysosome (El-Shewy and Luttrell, 2009; Urayama, 2013), the strong affinities of both ETV:IDS and IgG:IDS for M6PR suggest that the molecules are functionally similar with respect to M6PR binding (ELISA; Fig. 1 D), and therefore their M6PR-related trafficking is expected to be similar.

Interaction of both architectures with TfR is a critical attribute aimed at enabling brain uptake. Binding to TfR for ETV:IDS and IgG:IDS was assessed using two methods: monovalent affinities were determined by measuring binding to the soluble apical domain of human TfR (TfR[apical]), and apparent affinities arising from potential avid interactions with homodimeric TfR on the cell surface were approximated by measuring binding to full-length TfR immobilized at a high density. ETV:IDS displayed affinities between 100 and 200 nM regardless of assay format (Fig. 1 E), consistent with its ability to engage a single TfR. IgG:IDS can bind TfR bivalently and was strongly influenced by receptor density, having an affinity of 2.6 nM to TfR[apical] and an apparent affinity of <100 pM to the full-length receptor (Fig. 1 E). ETV:IDS and IgG:IDS were shown to compete for TfR binding (Fig. S1 A), indicating engagement with the receptor at overlapping epitopes. These values highlight the TfR affinity differences between the platforms and are in close agreement with previously reported results for ETV:IDS (Ullman et al., 2020) and for an anti-TfR antibody IDS fusion protein (Sonoda et al., 2018). Overall, IgG:IDS exhibited a monovalent affinity that was ~80-fold higher for TfR than ETV:IDS and the potential to bind TfR bivalently, leading to an apparent affinity ~1,000-fold greater than that of ETV:IDS.

The in vitro attributes quantified here between ETV:IDS and IgG:IDS demonstrate that although there may be modest differences in activity and cellular potency, the most substantial differences between these platforms are in TfR affinity and valency. The approximately twofold reduction in cellular potency observed for IgG:IDS, despite its higher specific activity compared with ETV:IDS, is most likely due to the effect of architecture on cellular uptake and trafficking. We hypothesized that differences in TfR affinity and valency would result in significantly different CNS biodistribution and efficacy for ETV:IDS and IgG:IDS in vivo.

ETV:IDS has enhanced peripheral exposure and improved brain uptake compared with IgG:IDS in TfR[mu/hu] KI mice
We next assessed the pharmacokinetic (PK) profiles of ETV:IDS and IgG:IDS in a chimeric mouse knock-in (KI) model expressing the human TfR[apical] domain (TfR[mu/hu] KI; Kariolis et al., 2020). Molecules with high affinity to TfR such as IgG:IDS have historically been dosed at 1–3 mg/kg (Sonoda et al., 2018; Zhou et al., 2012), whereas low-affinity TfR binders have often been evaluated at much higher doses ranging from 20 to 50 mg/kg

(Webster et al., 2017). These different dosing paradigms have led to the misperception that weaker TfR binding requires elevated doses to achieve brain exposures needed for a therapeutic response (Pardridge, 2015). Moreover, the reduced brain uptake often observed for high-affinity molecules at high doses has been suggested to be due to receptor saturation (Pardridge, 2015). It has been estimated that most LSDs likely only require a threshold of ~10% or less of normal residual enzyme activity to achieve full prevention of substrate storage and significant slowing of disease progression (Parenti et al., 2015). As long as enzyme formats achieve fairly uniform brain exposure that reliably extends beyond cerebral capillary endothelial cells, lower doses may therefore be sufficient to effectively reduce storage and disease progression.

To better understand the impact of dose on PK and biodistribution for the two platforms, TfR[mu/hu] KI mice received an intravenous (IV) dose of 1, 3, or 10 mg/kg ETV:IDS or IgG:IDS. Serum, liver, and brain concentrations of each molecule were determined to characterize biodistribution in key compartments (Ullman et al., 2020). Serum concentrations of ETV:IDS were elevated and more prolonged across dose levels compared with IgG:IDS (Fig. 2 A), consistent with TfR-mediated disposition from the circulation based on the strong, bivalent apparent affinity of IgG:IDS, whereas IgG:IDS liver levels exceeded those of ETV:IDS (Fig. 2 B). Importantly, ETV:IDS had 1.6- and 2.5-fold higher whole brain exposures compared with IgG:IDS at both 3 and 10 mg/kg, respectively (Fig. 2 C and Table S1). Maximal brain concentrations for ETV:IDS were 1.7- and 2.7-fold higher compared with IgG:IDS at both 3 and 10 mg/kg, respectively, 8–24 h after dose (Fig. 2 C and Table S1). In addition, IgG:IDS brain uptake appeared to plateau at 3 mg/kg, suggesting that this architecture saturates its uptake mechanism at low concentrations and therefore does not display the dose-dependent brain uptake that is evident for ETV:IDS. Indeed, ETV:IDS continued to show nonsaturable dose-dependent brain uptake up to 10 mg/kg (Fig. 2 C). An effective delivery platform for IDS should ideally provide dose-dependent exposure capable of reaching therapeutic efficacy in both the periphery and brain. Although the PK data for ETV:IDS satisfied these desired attributes, IgG:IDS exhibited higher peripheral clearance and an upper limit on whole brain exposure. Additional PK parameters are provided in Table S1.

ETV:IDS distributes more effectively into the brain parenchyma than IgG:IDS in TfR[mu/hu] KI mice
A limitation in assessing biodistribution to the brain using whole tissue lysates (Fig. 2 C) is that this approach does not differentiate between accumulation in the vasculature versus the parenchyma, making it difficult to distinguish actual transcytosis at the BBB from entrapment in capillary endothelial cells. Because it is well established that TfR-targeted proteins and nanoparticles may become trapped within brain capillary endothelial cells under some conditions (Bien-Ly et al., 2014; Johnsen et al., 2017; Manich et al., 2013; Moos and Morgan, 2001; Niewoehner et al., 2014; Paris-Robidas et al., 2011; Webster et al., 2017; Yu et al., 2011), we further assessed the brain biodistribution of ETV:IDS and IgG:IDS using brain capillary
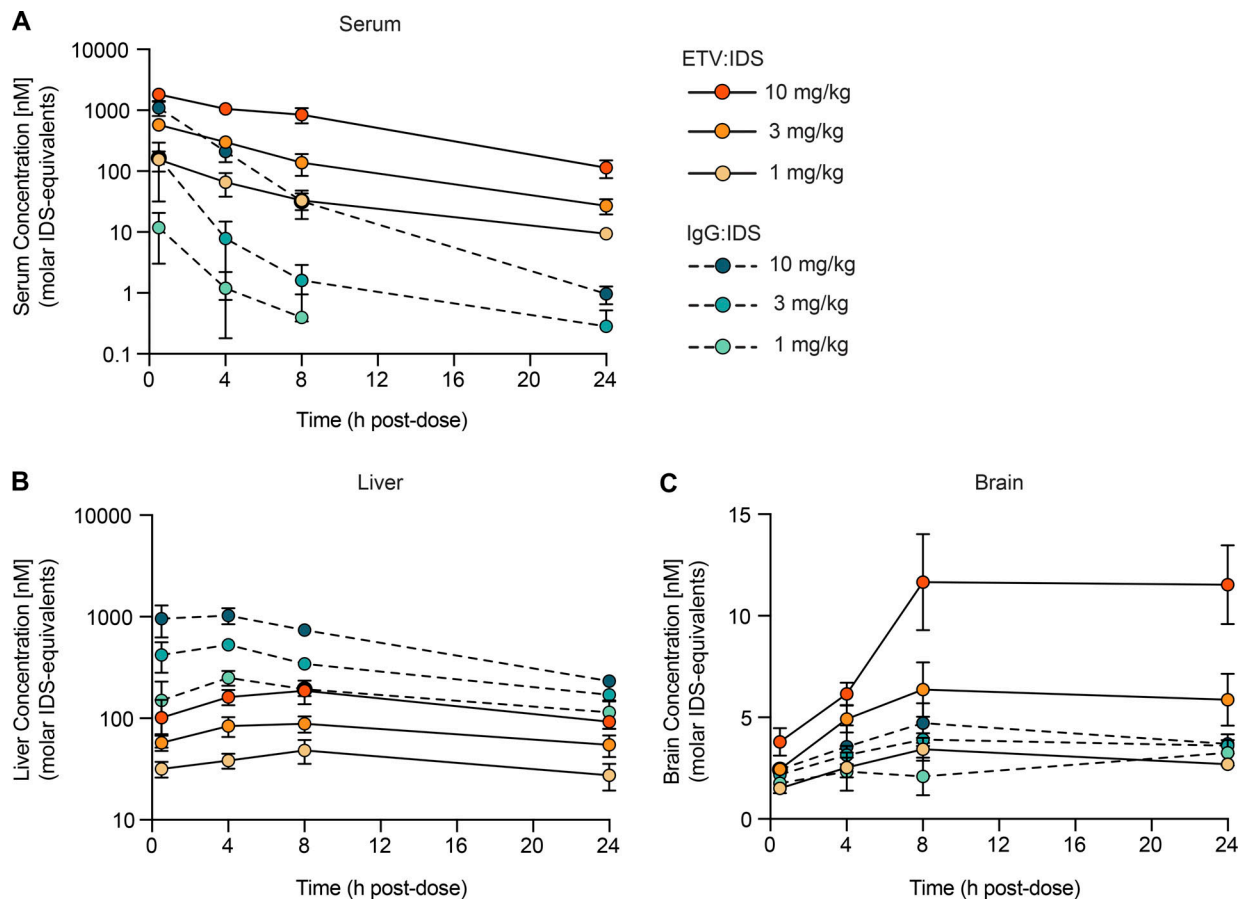
Figure 2. **ETV:IDS has improved brain uptake compared with IgG:IDS in TfR^mu/hu KI mice. (A–C)** Serum (A), liver (B), and brain (C) concentrations of ETV: IDS or IgG:IDS from TfR^mu/hu KI mice were measured 0.5, 4, 8, and 24 h after an IV dose of 1, 3, or 10 mg/kg and determined using an IDS capture/IDS detect immunoassay. TfR^mu/hu KI mice are on a C57BL/6 background. Data presented are from a single study. ELISA data represent the average of $n = 2$ technical replicates per mouse; each symbol represents an average of $n = 3–5$ mice per group per time point; graphs display mean ± SD.

depletion. The capillary depletion method isolates brain vasculature from whole brain homogenate, allowing for a concentration determination in separate vascular and parenchymal fractions (Triguero et al., 1990). We used this method to evaluate the distribution of ETV:IDS and IgG:IDS into the brain 0.5, 4, and 24 h after an IV dose in TfR^mu/hu KI mice (10 mg/kg). Notably, IDS concentrations in the brain vascular fraction for IgG:IDS increased at each time point, whereas a minimal change for ETV: IDS was observed over time (Fig. 3 A). In contrast, IDS levels in the parenchymal fraction steadily increased with time for ETV: IDS, and IgG:IDS levels remained low over the entire 24 h, resulting in 3.5- and 4-fold higher concentrations obtained with ETV:IDS compared with IgG:IDS 4 and 24 h after dose (Fig. 3 B). Expressing the data as a ratio of the parenchymal-to-vascular concentrations provided a further measure of distribution into the parenchyma, taking into account the IDS level in each fraction simultaneously (Fig. 3 C). This ratio increased significantly over time for ETV:IDS, with the 4- and 24-h time points 26% and 165% higher, respectively, than the initial 0.5-h value, whereas the IgG:IDS ratio was significantly lower than the ETV: IDS ratio at 0.5 h and failed to increase over time (Fig. 3 C). The low brain parenchymal fraction measured over 24 h for IgG:IDS

is consistent with other reports using a similar fusion protein (Sonoda et al., 2018). The data suggest that ETV:IDS effectively crossed the BBB with subsequent distribution into the brain parenchyma, whereas IgG:IDS was primarily trapped within the brain vasculature.

The precise molecular mechanisms underlying TfR-mediated transcytosis remain to be fully elucidated (Villasenor et al., 2019). Bivalent receptor interactions appear to drive TfR cross-linking and clustering at the brain endothelial cell luminal membrane, increasing uptake and lysosomal degradation while decreasing recycling, due partly to differential sorting within the endocytic pathway (Niewoehner et al., 2014; Villasenor et al., 2017; Weflen et al., 2013). High-affinity interactions with TfR, regardless of valency, also appear to lead to increased lysosomal trafficking of biotherapeutics in brain endothelial cells (Bien-Ly et al., 2014; Haqqani et al., 2018; Yu et al., 2011). Our capillary depletion data are consistent with these mechanisms. We show with ETV:IDS that decreasing affinity and restricting TfR binding to a monovalent interaction resulted in significantly higher distribution into the brain parenchyma, compared with IgG:IDS, which distributed primarily within the brain vasculature.
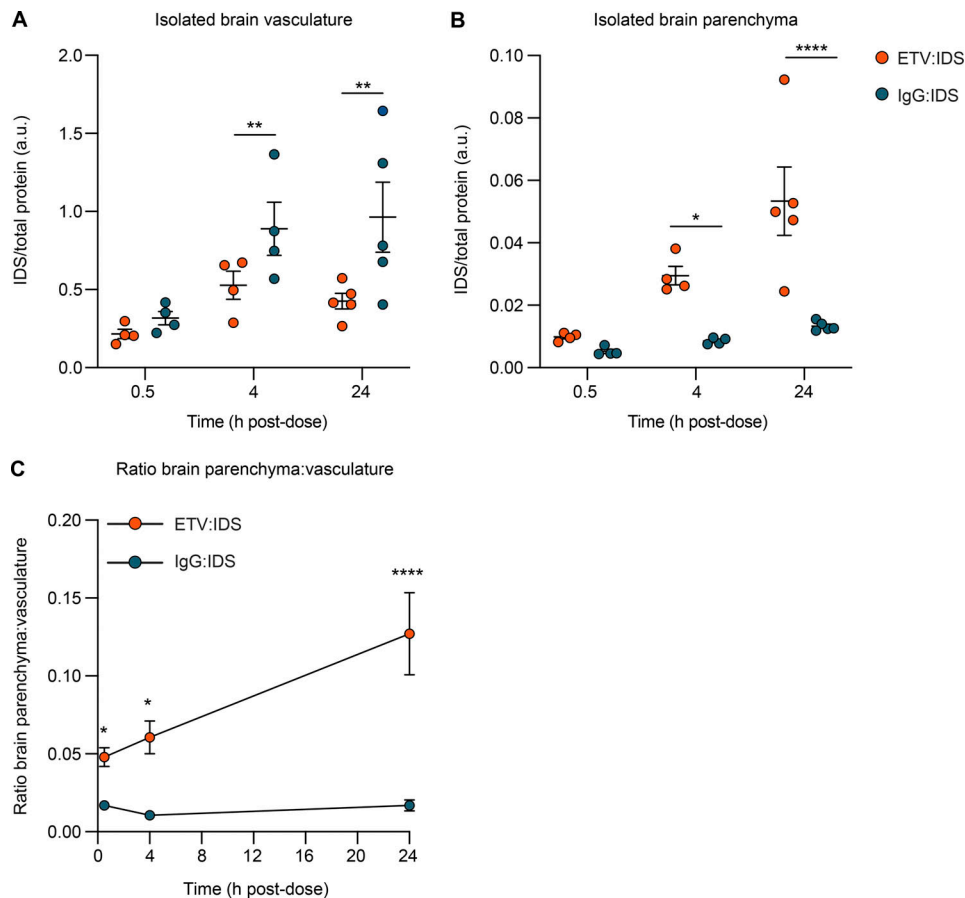
A Isolated brain vasculature

B Isolated brain parenchyma

C Ratio brain parenchyma:vasculature

Figure 3. **Capillary depletion method demonstrates accumulation of ETV:IDS in the brain parenchyma and IgG:IDS in the brain vasculature. (A and B)** Concentrations of ETV:IDS or IgG:IDS in the isolated brain vasculature (A) or brain parenchymal fraction (B) from TfR$^{mu/hu}$ KI mice were measured 0.5, 4, and 24 h after an IV dose of 10 mg/kg and determined using an IDS capture/IDS detect immunoassay. TfR$^{mu/hu}$ KI mice are on a C57BL/6 background. Data presented are from a single study. ELISA data represents the average of $n = 2$ technical replicates per mouse; each symbol represents a biological replicate with $n = 4–5$ mice per group. **(C)** Ratio of brain parenchyma to brain vasculature concentrations. Data presented are from a single study. ELISA data represent the average of $n = 2$ technical replicates per mouse; each symbol represents an average of $n = 4–5$ mice per group per time point. Graphs display mean ± SEM and P values: two-way ANOVA with Sidak's multiple comparison test; *, $P ≤ 0.05$; **, $P ≤ 0.01$; ****, $P ≤ 0.0001$. a.u., arbitrary unit.

Imaging demonstrates that ETV:IDS enables greater parenchymal distribution, neuronal uptake, and trafficking to parenchymal lysosomes than IgG:IDS in TfR$^{mu/hu}$ KI mice

Quantitative imaging methods and SRCM were used to confirm the capillary depletion results and better understand the brain distribution of ETV:IDS and IgG:IDS at the regional, cellular, and subcellular levels. Imaging was performed on sagittal brain sections from TfR$^{mu/hu}$ KI mice 0.5, 4, and 24 h after an IV dose (10 mg/kg). Brain sections were immunostained for human IgG (huIgG), and imaging was performed on multiple different brain regions (Figs. 4 A and S2). The antibody used to detect huIgG was shown to bind to IgG:IDS and ETV:IDS similarly (Fig. S1 B). Qualitative assessment of huIgG staining in the cortex of mice after administration of IgG:IDS demonstrated a predominantly vascular pattern at all time points (Fig. 4 A). Conversely, after ETV:IDS administration, huIgG staining in the cortex of mice was predominantly vascular at 0.5 h but transitioned to a broad, diffuse parenchymal pattern with prominent cellular internalization by 24 h (Fig. 4 A). Quantitative analysis of extravascular huIgG staining in the cortex confirmed ETV:IDS signal

accumulation in the brain parenchyma over time, with the 4 and 24 h time points 30% and 54% higher, respectively, than the initial 0.5-h value (Fig. 4 B). This contrasted with a relatively low and constant extravascular huIgG signal for IgG:IDS (Fig. 4 B), in general agreement with capillary depletion results. Furthermore, expressing the data as a ratio of the normalized huIgG signal in the brain parenchyma to brain vasculature showed increased distribution of ETV:IDS into the brain parenchyma from 0.5 to 24 h, while the IgG:IDS ratio was lower than ETV:IDS and failed to increase over time (Fig. 4 B). A similar staining pattern and quantification was also observed for both molecules in all other regions assessed, including the hippocampus, hindbrain, and cerebellum (Fig. S2).

SRCM was used to investigate the subcellular localization of huIgG staining in brain sections from the cortex of TfR$^{mu/hu}$ KI mice following an IV dose (10 mg/kg) of ETV:IDS or IgG:IDS at 24 h after dose, when staining differences were most pronounced. Imaging at subcellular resolution and subsequent segmentation of huIgG-positive signal into vascular and parenchymal components revealed a more prominent, diffuse
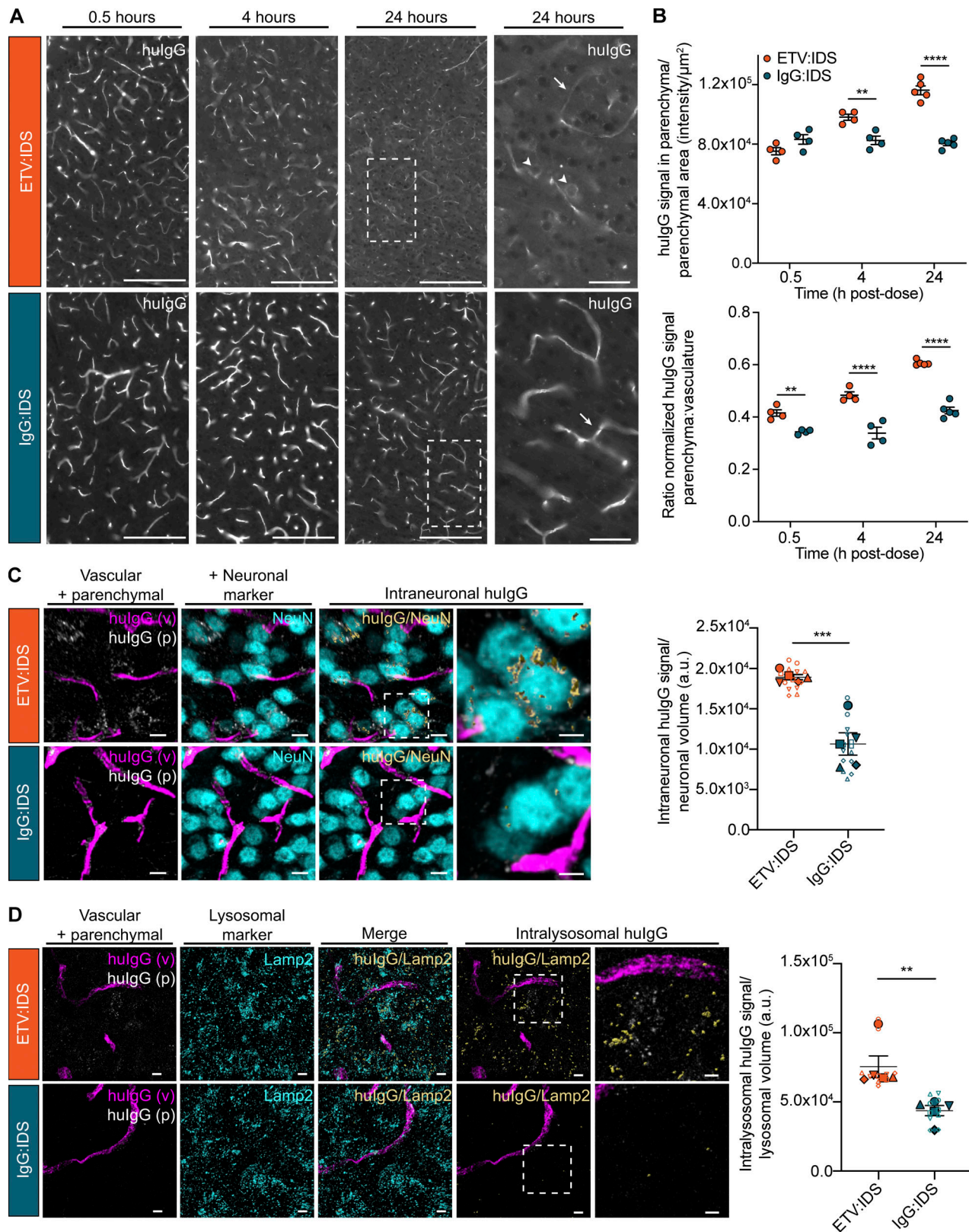
Figure 4. **IHC localization of ETV:IDS demonstrates enhanced distribution into the brain parenchyma compared with IgG:IDS.** The distribution of ETV: IDS and IgG:IDS was assessed using sagittal brain sections from TfR$^{mu/hu}$ KI mice 0.5, 4, and 24 h after an IV dose of 10 mg/kg. TfR$^{mu/hu}$ KI mice are on a C57BL/6 background. Schematic indicating approximate location of sagittal brain regions of interest (ROIs) for images and quantification is in Fig. S2 A. **(A)** Sections were immunostained with antibodies against huIgG, imaged, and post-stitched using a wide-field fluorescence slide scanner. Scale bars = 200 μm. Dashed boxes indicate cortical regions shown at higher magnification displayed in the far-right panel; scale bars = 50 μm. Arrows indicate huIgG staining localized to vascular profiles; arrowheads indicate cellular internalization of huIgG staining. **(B)** Quantification of huIgG staining in the parenchyma of the cortex was

calculated based on the total sum intensity of all parenchymal staining in the ROI divided by the total parenchymal area in the ROI. A custom macro script was used to identify blood vessels present in the tissue and masked out of subsequent image analyses. The ratio of normalized huIgG signal in the brain parenchyma to brain vasculature was also quantified. Data presented are from a single study with n = 4–5 mice per group. Each symbol represents a biological replicate. Graphs display mean ± SEM and P values: two-way ANOVA with Sidak's multiple comparison test; **, P ≤ 0.01; ****, P ≤ 0.0001. **(C and D)** Sagittal brain sections from TfR$^{mu/hu}$ KI mice 24 h after an IV dose of 10 mg/kg were immunostained with antibodies against huIgG and the neuronal marker NeuN (C) or huIgG and the endolysosomal marker LAMP2 (D). Confocal Z-stacks were acquired using SRCM. Scale bars = 10 μm. Dashed boxes indicate cortical regions shown at higher magnification displayed in the far-right panel; scale bars = 5 μm. For the analysis, huIgG-positive signal was segmented into vascular (magenta) and parenchymal (grayscale) components. Intraneuronal huIgG (yellow, shown with surface rendering; C) and intralysosomal huIgG (yellow, shown with surface rendering; D) was further segmented using either NeuN or LAMP2 (cyan) as a mask. In D, the merged panel shows both LAMP2 signal non-colocalized (cyan) and colocalized (yellow, shown with surface rendering) with huIgG signal. For better visualization, the subsequent intralysosomal panels show only the parenchymal LAMP2 signal that colocalized with huIgG (yellow). The intraneuronal (C) and intralysosomal (D) huIgG signal was quantified and normalized to the total neuronal volume or total lysosomal volume, respectively. Data presented are from a single study with n = 5 mice per group. Graphs display superimposed summary statistics from n = 5 mice (solid shapes) consisting of two to three different image volumes from each animal (open shapes). Each animal is coded by different shapes. The five means were then used to calculate the mean ± SEM and P values: unpaired t test analysis; **, P ≤ 0.01; ***, P ≤ 0.001. a.u., arbitrary unit.

parenchymal staining pattern for ETV:IDS compared with IgG:IDS (Fig. 4, C and D, leftmost panels). Treatment with ETV:IDS also resulted in significantly greater huIgG signal in NeuN-positive cortical neurons compared with IgG:IDS (Fig. 4 C); our use of SRCM demonstrating robust uptake of ETV:IDS into neurons is consistent with prior results reporting ETV:IDS uptake and effects in neurons using flow cytometry–based methods (Ullman et al., 2020). As LSDs lead to progressive substrate accumulation and perturbed lysosomal function, we also compared parenchymal cell internalization and trafficking to lysosomes for ETV:IDS and IgG:IDS. Consistent with increased distribution to cortical neurons, treatment with ETV:IDS resulted in significantly greater cortical huIgG signal in lysosome-associated membrane protein 2 (LAMP2)–positive endolysosomes compared with IgG:IDS (Fig. 4 D).

Our use of native, unlabeled molecules for quantitative imaging and SRCM avoided possible confounding effects associated with labeled molecules (e.g., fluorophores, colloidal gold, or peroxidase conjugates), since labels may complicate interpretation of TfR-targeted trafficking at the BBB (Bickel et al., 1994). Quantitative SRCM also has advantages over more qualitative, historical methods for studying subcellular distribution such as EM. Taken together, our imaging results demonstrate that ETV:IDS was superior to IgG:IDS in achieving brain exposure beyond the vasculature, with broad distribution across brain regions, internalization into neurons, and lysosomal trafficking in brain cells. In contrast, IgG:IDS was predominantly within the brain vasculature, resulting in limited uptake into neurons and poor lysosomal trafficking in brain cells. The results therefore demonstrate that the two architectures yield significant differences in CNS biodistribution.

ETV:IDS dose-dependently reduces brain GAG levels compared with IgG:IDS in Ids KO; TfR$^{mu/hu}$ KI mice

We next investigated whether the higher whole brain exposures with ETV:IDS compared with IgG:IDS in TfR$^{mu/hu}$ KI mice translated to more effective CNS GAG reduction in a mouse model of MPS II (Ids KO;TfR$^{mu/hu}$ KI; Ullman et al., 2020). Mice received an IV dose of ETV:IDS or IgG:IDS at 1, 3, or 10 mg/kg, and GAG levels in liver, CSF, and brain were assessed after 7 d. Both ETV:IDS and IgG:IDS were highly effective peripherally, reducing liver GAGs to TfR$^{mu/hu}$ KI levels (Fig. 5 A). In the CSF,

ETV:IDS dose-dependently lowered GAGs by 68–80% compared with the vehicle treatment group, whereas IgG:IDS decreased CSF GAGs by 32–61% over the same dose range (Fig. 5 B and Table S2). In brain tissue lysate, ETV:IDS significantly lowered GAG concentrations over the entire dose range (49–76% reduction), whereas IgG:IDS decreased GAGs to a substantially lesser extent (25–43%; Fig. 5 C and Table S2).

Taken together, this head-to-head comparison of two clinically relevant IDS fusion protein architectures provides new evidence indicating how differences in TfR engagement can lead to significant and divergent effects on brain distribution and, ultimately, pharmacodynamics in vivo. Significant brain GAG reduction over the 1–10 mg/kg dose range for ETV:IDS was consistent with its superior biodistribution to the brain in TfR$^{mu/hu}$ KI mice. Unlike IgG:IDS, ETV:IDS appeared to undergo pronounced transcytosis across brain endothelial cells to more effectively reach neurons and lysosomal compartments within the brain parenchyma, building on recent evidence using other methods (Ullman et al., 2020). For IgG:IDS, the lack of dose-dependent brain uptake and GAG reduction in mouse models is consistent with poor trafficking across the BBB and inferior biodistribution to brain cells and limits the feasibility of exploring higher dose levels with an IgG:IDS architecture. The brain GAG reduction differences observed between ETV:IDS and IgG:IDS also agree well with our capillary depletion and imaging data, suggesting that TfR engagement-dependent effects are most likely responsible for their differing efficacy. The size difference between ETV:IDS (~110 kD) and IgG:IDS (~265 kD) also may have subtly affected their relative biodistribution in brain extracellular space within and beyond the vascular basal lamina, although interstitial diffusion outward from capillaries is generally not expected to be highly limiting for molecules of this size (Wolak et al., 2015; Wolak and Thorne, 2013).

Our results also suggest that CSF biomarker changes such as GAG reduction may accurately reflect pharmacodynamic effects in the brain only for IDS platforms in which both preclinical distribution to brain parenchymal cells and corresponding effects on brain GAG reduction can be convincingly demonstrated, as reported here for ETV:IDS. Ultimately, further definitive insights into the relative advantages of diverse TfR-targeting brain delivery platforms may be provided only by the demonstration of efficacy in human patients. From the preclinical data
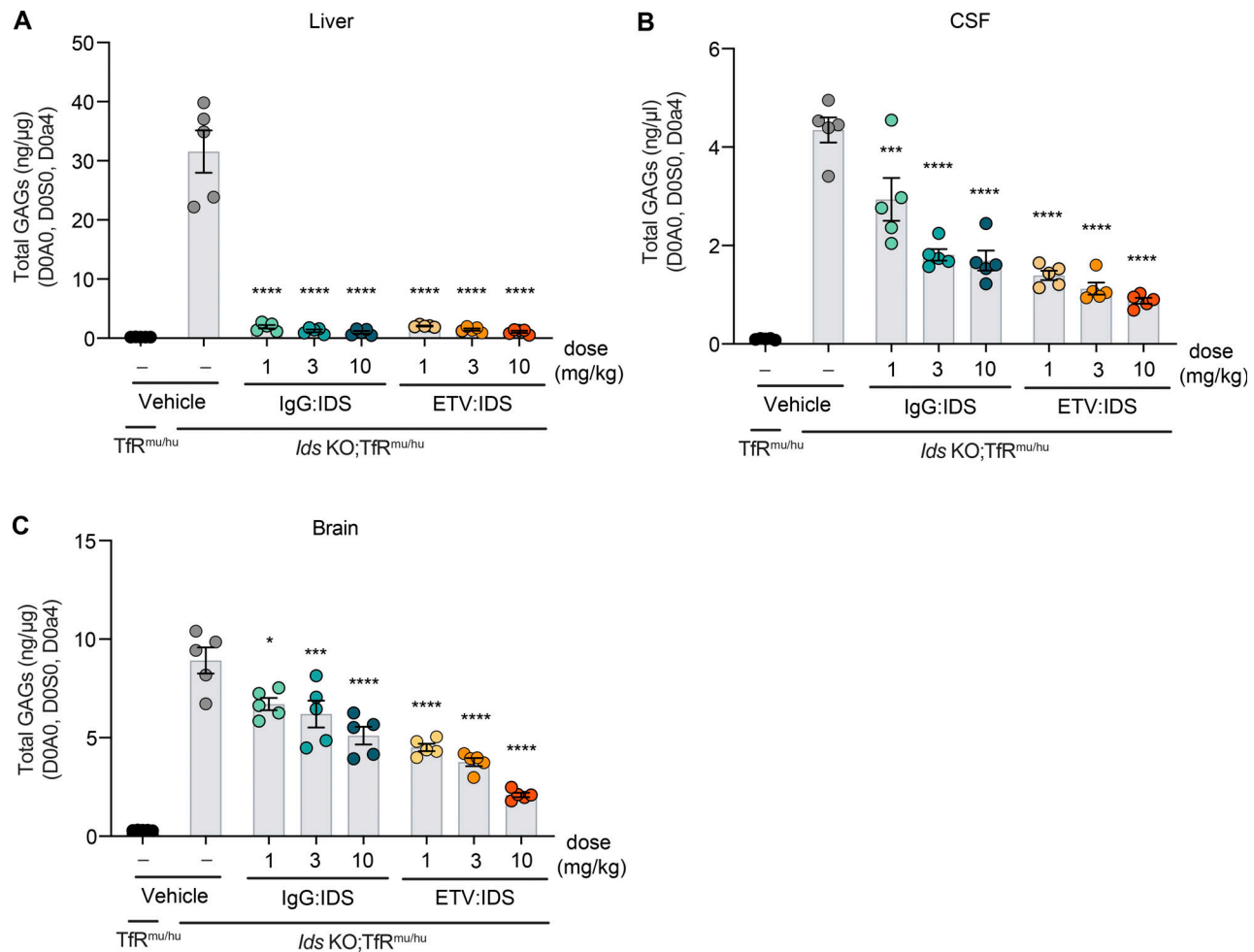
Figure 5. ETV:IDS is more effective than IgG:IDS at reducing brain and CSF GAGs in _Ids_ KO;TfR[mu/hu] KI mice. (A–C) GAG levels were evaluated in the liver (A), CSF (B), and brain (C) of _Ids_ KO;TfR[mu/hu] KI mice 7 d after treatment with ETV:IDS or IgG:IDS after an IV dose of 1, 3, or 10 mg/kg and compared with vehicle treatment and nondiseased littermate control TfR[mu/hu] KI mice. All mice are on a C57BL/6 background. Data presented are from a single study with _n_ = 5 mice per group. Each symbol represents a biological replicate. Graphs display mean ± SEM and P values: one-way ANOVA with Tukey's multiple comparison test; *, P ≤ 0.05; ***, P ≤ 0.001; ****, P ≤ 0.0001.

described here, understanding the impact of binding mode between the biotherapeutic and the receptor may prove to be a key consideration in successful clinical translation.

Materials and methods

Cloning and architecture of ETV:IDS and IgG:IDS

All material used in this study was produced for research purposes. ETV:IDS was expressed as a knob-in-hole recombinant fusion protein consisting of IDS fused at the C-terminus (via a peptide linker) to a single copy of human Fc engineered to bind hTfR (Kariolis et al., 2020). IgG:IDS was expressed as a recombinant fusion protein consisting of an anti-TfR mAb fused at the C-terminus (via a peptide linker) of each heavy chain to IDS (CAS#2140211-48-7). Antibody constant regions used were human IgG1. Mutations mitigating effector function (L234A and L235A) were included on ETV:IDS (Kariolis et al., 2020), whereas effector function was maintained on IgG:IDS as described (L234 and L235; Sonoda et al., 2018).

Protein expression

The IgG:IDS construct was expressed via transient transfection of ExpiCHO cells (Thermo Fisher Scientific) according to manufacturer's instructions. Cultures were cotransfected with plasmids encoding IgG:IDS (heavy chain and light chains) and varying ratios of SUMF1 cDNAs. ETV:IDS was purified from a stable Chinese hamster ovary (CHO) clone.

Protein purification

ETV:IDS and IgG:IDS were purified to homogeneity from serum-free CHO cultures by a series of chromatographic steps. IgG:IDS was affinity purified using Protein A followed by anion-exchange chromatography. Final fractions with a high degree of purity (as assessed by analytical size-exclusion chromatography and/or microcapillary electrophoresis) were pooled, concentrated, and dialyzed into 20 mM sodium phosphate, pH 6.5, and 130 mM NaCl. ETV:IDS was purified by a three-step chromatographic approach: Protein A affinity followed by anion exchange and finally hydrophobic interaction chromatography.

Preparations were stored at 4°C or –80°C before use and routinely analyzed by size-exclusion chromatography and specific activity and for endotoxin content.

Biochemical characterization

K_D determination using surface plasmon resonance

The affinity of ETV:IDS and IgG:IDS for hTfR was determined by surface plasmon resonance on a Biacore T200 instrument using two methods, similar to those previously described (Kariolis et al., 2020). In method 1, to evaluate monovalent TfR binding affinities, ETV:IDS or IgG:IDS was captured on a Protein A–coated Biacore Series S CM5 sensor chip, and serial dilutions of hTfR^{apical} were injected over the captured sample. In method 2, for evaluation of apparent hTfR binding affinities of ETV:IDS and IgG:IDS, biotinylated full-length hTfR was immobilized on a streptavidin-coated CM5 sensor chip, followed by injection of serial dilutions of ETV:IDS or IgG:IDS. For both methods, the single-cycle kinetics mode was used for sample injection (association time, 90 s; dissociation time, 600 s), and binding affinities were calculated using Biacore T200 software v3.0.

Human TfR-binding competition assay

Competition of ETV:IDS and IgG:IDS for hTfR binding was assessed using biolayer interferometry. Biolayer interferometry experiments were performed on an Octet RED384 (Sartorius) instrument at 25°C. All the samples were diluted with Kinetics buffer (18-1092; Sartorius) and transferred to solid-black 384-well plates (781900; Greiner Bio-One). Streptavidin-coated biosensors (18-5021; Sartorius) were loaded with biotinylated recombinant human TfR ECD for 400 s. TfR binding antibody, IgG:IDS, and ETV:IDS were subsequently loaded for 1,100 s on surface-bound TfR followed by ETV:IDS loading for hTfR-binding competition.

In vitro IDS activity assay

The specific activity of IDS-containing constructs was measured with a two-step fluorometric enzymatic assay using an artificial substrate as previously described (Voznyi et al., 2001). In brief, a 4-methylumbelliferone (leaving group) standard curve was fitted by linear regression to calculate the amount of product and verified as <10% of total substrate cleavage. Specific activity calculated as picomoles of product per minute per milligram of protein was determined.

ELISA-based analysis of M6PR binding

ELISA plates were coated with M6PR Fc at 1 µg/ml in PBS overnight at 4°C. The next day, the plate was washed three times with wash buffer (PBS with 0.02% Tween-20), and blocking buffer (PBS with 0.02% Tween-20 and 5% BSA) was added to each well. Blocking was carried out for 1 h at room temperature, after which the plate was washed three times, and ETV:IDS or IgG:IDS was added to the first column of the plate at a concentration of 25 nM. A threefold serial dilution was performed across the plate. Primary incubation of the binding reactions was done for 1 h at room temperature. After binding, the plate was washed three times, and binding was detected using biotinylated anti-IDS antibody diluted to 0.0625 µg/ml in sample

buffer. The plate was incubated with detection antibody for 1 h at room temperature and then washed three times. Streptavidin-HRP, diluted 1:50,000 in sample buffer, was then added to each well. The plate was incubated for 30 min at room temperature and then washed three times. The ELISA was developed using 3,3′,5,5′tetra-methyl-benzidine (TMB) reagent. The ELISA plate was read on a HighRes BioTek Synergy plate reader, and the absorbance at 450 nm was recorded.

ELISA-based analysis of huIgG binding

Binding of the anti-huIgG polyclonal antibody to IgG:IDS and ETV:IDS that was used for immunohistochemistry (IHC) was measured by ELISA. Anti-IDS pAb (AF2449; R&D Systems) was used to coat the ELISA plate at a concentration of 2 µg/ml in PBS overnight at 4°C. The next day, the plate was washed three times with wash buffer (PBS with 0.02% Tween-20), and blocking buffer (PBS with 5% BSA) was added to each well. Blocking was carried out for 1 h at room temperature, after which the plate was washed three times, and ETV:IDS or IgG:IDS was added to the first column of the plate at a concentration of 200 nM. A fourfold serial dilution was performed across the plate. Primary incubation of the binding reactions was done for 1 h at room temperature. After binding, the plate was washed three times, and binding was detected using biotinylated anti-huIgG antibody (109-065-003; Jackson ImmunoResearch; biotinylated version of the antibody used for IHC) diluted to 0.05 µg/ml in sample buffer. The plate was incubated with detection antibody for 1 h at room temperature and then washed three times. Streptavidin-HRP, diluted 1:50,000 in sample buffer, was then added to each well. The plate was incubated for 30 min at room temperature and then washed three times. The ELISA was developed using TMB reagent. The ELISA plate was read on a HighRes BioTek Synergy plate reader, and the absorbance at 450 nm was recorded.

[S^{35}]sulfate accumulation assay to assess cellular potency

Cellular potency of IgG:IDS and ETV:IDS was carried out as described previously (Ullman et al., 2020). MPS II patient (GM01928, GM12366, and GM13203) primary fibroblasts were obtained from Coriell. The cellular S^{35}-accumulation assay was performed using a method modified from Lu et al. (2010). Briefly, fibroblasts were plated at 25,000 cells/well in 96-well plates and grown in DMEM high glucose (Gibco) with 10% FBS (Sigma-Aldrich). After 3 d of culture, medium was replaced with low-sulfate F12 medium (Gibco) supplemented with 10% dialyzed FBS and 40 mCi/ml [S^{35}]sodium sulfate (PerkinElmer) for 96 h. After [S^{35}]sodium sulfate incubation, cells were treated with ETV:IDS or IgG:IDS. After 24 h of incubation, medium was aspirated, and cells were washed with cold PBS and lysed with 0.01 N NaOH. Incorporated S^{35} was measured by scintillation counting (Microbeta Trilux). IC$_{50}$ curves were generated using Prism software using a log(agonist) versus response, variable slope (four-parameter) fit.

Animal care

All procedures in animals were performed with adherence to ethical regulations and protocols approved by Denali

Arguello et al.
Architecture determines brain delivery of enzymes

Journal of Experimental Medicine 10 of 15
https://doi.org/10.1084/jem.20211057

Therapeutics Institutional Animal Care and Use Committee. Mice were housed under a 12-h light/dark cycle and had access to water and standard rodent diet (#25502, irradiated; LabDiet) ad libitum.

Mouse strains

A previously described *Ids* KO mouse model on a B6N background was obtained from The Jackson Laboratory, JAX strain 024744 (Muenzer et al., 2002). The TfR$^{mu/hu}$ KI mouse line harboring the human TfR apical domain knocked into the mouse receptor was developed by generating a KI (into C57Bl6 mice) of the human apical TfR mouse line via pronuclear microinjection into single-cell embryos, followed by embryo transfer to pseudo-pregnant females using CRISPR/Cas9 technology. The donor DNA comprised the human TfR apical domain coding sequence that has been codon optimized for expression in mouse. The resulting chimeric TfR was expressed in vivo under the control of the endogenous promoter. A founder male from the progeny of the female that received the embryos was bred to wild-type females to generate F1 heterozygous mice. Homozygous mice were subsequently generated from breeding of F1-generation heterozygous mice (Kariolis et al., 2020). TfR$^{mu/hu}$ KI male mice were bred to female *Ids* heterozygous mice to generate *Ids* KO; TfR$^{mu/hu}$ KI mice (Ullman et al., 2020). All mice are on a C57BL/6 background, and all mice used in this study were males.

Biodistribution and PK of ETV:IDS and IgG:IDS

ETV:IDS or IgG:IDS was administered IV via the tail vein to 2–3-mo-old TfR$^{mu/hu}$ KI mice (n = 3–5 per group) at doses of 1, 3, or 10 mg/kg body weight, and animals were sacrificed at 0.5, 4, 8, and 24 h after dose. For terminal sample collection, animals were deeply anesthetized via i.p. injection of 2.5% Avertin. Blood was collected via cardiac puncture for serum collection and allowed to clot at room temperature for ≥30 min. Tubes were then centrifuged at 12,700 rpm for 7 min at 4°C. Serum was transferred to a fresh tube and flash-frozen on dry ice. Animals were transcardially perfused with ice-cold PBS using a peristaltic pump (Minipuls Evolution; Gilson) and the liver and brain were dissected. Liver and brain tissue (50 mg) were flash-frozen on dry ice and processed for an IDS:IDS ELISA as described below. Brain tissue from the 10-mg/kg groups were processed for capillary depletion and IHC, as described below.

Pharmacodynamics of ETV:IDS and IgG:IDS

ETV:IDS or IgG:IDS were administered IV via the tail vein to 2–3-mo-old TfR$^{mu/hu}$ KI mice (n = 5 per group) and *Ids* KO;TfR$^{mu/hu}$ mice (n = 5 per group) at doses of 0, 1, 3, or 10 mg/kg weight, and animals were sacrificed 7 d after dose. For terminal sample collection, animals were deeply anesthetized via i.p. injection of 2.5% Avertin. For CSF collection, a sagittal incision was made at the back of the animal's skull, subcutaneous tissue and muscle was separated to expose the cisterna magna, and a pre-pulled glass capillary tube was used to puncture the cisterna magna to collect CSF. CSF was transferred to a Low Protein LoBind Eppendorf tube and centrifuged at 12,700 rpm for 10 min at 4°C. CSF was transferred to a fresh tube and snap frozen on dry ice. Lack of blood contamination in mouse CSF was

confirmed by measuring the absorbance of the samples at 420 nm. Blood, serum, and tissues were obtained as described and flash frozen on dry ice.

Tissue processing for PK analysis

Tissue (50 mg) was homogenized in 10× volume by tissue weight cold 1% NP-40 lysis buffer (1 ml 10% NP-40 Surfact-Amps detergent solution, 9 ml of 1× PBS, 1 tablet cOmplete protease inhibitor, and 1 tablet PhosSTOP protease inhibitor) with a 3-mm stainless steel bead using the Qiagen TissueLyzer II for two rounds of 3 min at 27 Hz. Homogenates were then incubated on ice for 20 min and spun at 14,000 rpm for 20 min at 4°C. The resulting lysate was transferred to a single-use aliquot and stored at –80°C.

IDS:IDS ELISAs and PK analysis

ETV:IDS and IgG:IDS were measured in serum, liver lysates, and brain lysates using an iduronate-2-sulfatase sandwich ELISA. A 384-well Maxisorp plate (464718; Thermo Fisher Scientific) was coated overnight with an anti-IDS antibody (AF2449; R&D Systems) and blocked with Casein-PBS Buffer (37528; Thermo Fisher Scientific) the next day. Samples containing either ETV:IDS or IgG:IDS were added to the plate and incubated for 1 h at room temperature. After a subsequent wash, a biotinylated anti-IDS antibody (BAF2449; R&D Systems) was added to bind the immobilized ETV:IDS and IgG:IDS. The IDS sandwich was then detected with a streptavidin-HRP conjugate (016-030-084; Jackson ImmunoResearch) followed by incubation with TMB substrate (34028; Thermo Fisher Scientific). The reaction was quenched with 4 N hydrosulfuric acid (SS04; Life Technologies), and the plate was read at 450-nm absorbance wavelength on a plate spectrophotometer to determine the concentrations of analyte in the samples. Calibration standard curves were generated for ETV:IDS and IgG:IDS using a 5-parameter logistic fit with an assay range of 0.00137–1 nM. Protein sequence–derived molecular weights were used to calculate molar concentrations. To compare ETV:IDS and IgG:IDS concentrations in terms of molar equivalents of IDS enzyme (Fig. 2), a correction factor was applied to IgG:IDS concentration data to account for the 2:1 ratio of IDS enzyme per mole of IgG:IDS (Fig. 1). Serum, liver, and brain area-under-the-curve exposures for ETV:IDS and IgG:IDS were calculated from corrected concentration data using non-compartmental analysis in Dotmatics, v4.8 (Bishop's Stortford). Serum clearance and steady-state distribution volume were determined by noncompartmental analysis using original molar concentration data. Semi-log and linear graphs and tabular results with SDs were prepared with Prism 8 (GraphPad).

Capillary depletion

Meninges and choroid plexuses were removed from the brain pieces reserved for capillary depletion immediately after extraction to ensure that these blood–CSF barriers did not contribute to an overestimation of IDS concentration in the isolated brain parenchyma samples. The capillary depletion method was conducted as previously described (Kariolis et al., 2020). Briefly, fresh brain pieces were homogenized on ice by 10 strokes with a Dounce homogenizer (smaller diameter pestle) in 3.5 ml HBSS

Arguello et al.
Architecture determines brain delivery of enzymes

Journal of Experimental Medicine   11 of 15
https://doi.org/10.1084/jem.20211057

and then centrifuged for 10 min at 1,000 g. The pellet was resuspended in 2 ml of 17% dextran (mol wt 60,000; 31397; Sigma-Aldrich) and centrifuged for 15 min at 4,122 g to separate the parenchymal cells from the vasculature. The top myelin and parenchymal cell layers were removed together and diluted with HBSS, then centrifuged for 15 min at 4,122 g to pellet the parenchymal cells. Both the vascular pellets and parenchymal cell pellets were resuspended in cold 1% NP40 in PBS with protease and phosphatase inhibitors (04693159001 and 04906837001; Sigma-Aldrich), agitated for 30 s at 27 Hz with a Tissue Lyser II (85300; Qiagen), and then incubated for 20 min on ice. The cell lysate was collected after centrifugation for 10 min at 12,700 g. The total protein concentration of each sample was measured using a BCA assay (23225; Thermo Fisher Scientific).

IHC
Immediately after extraction, mouse brain tissue was fixed in 4% paraformaldehyde for 24 h at 4°C and then transferred to 30% sucrose in 1× PBS for ≥24 h at 4°C. Sagittal tissue sections at 30-μm thickness were sectioned using a Leica Sliding Microtome. Free-floating sections were collected in 2-ml Eppendorf Tubes filled with 1× PBS with 0.05% sodium azide and either directly mounted onto Fisherbrand Superfrost Plus microscope slides or used as free-floating sections throughout the IHC process. Sections were rinsed in 1× PBS for two rounds of 5 min and then transferred to Sequenza Clips (for those sections directly mounted onto microscope slides) and rinsed in 1× PBS/0.05% Tween. Sections were permeabilized in 0.5% Triton X-100 for 15 min and incubated in Blocking Solution (1% BSA, 0.1% fish skin gelatin, 0.5% Triton X-100, and 0.1% sodium azide in 1× PBS) for 2 h at room temperature. Sections were incubated in primary antibody (109-605-003; Jackson ImmunoResearch: goat anti-huIgG conjugated to Alexa Fluor 647, 1:250, GL2A7; Abcam: rat anti-LAMP2, 1:500, EPR12763l Abcam: rabbit anti-NeuN, 1:500) prepared in Antibody Dilution Buffer (1% BSA and 0.1% sodium azide in 1× PBS) overnight at 4°C. Sections were rinsed in 1× PBS/0.05% Tween for three rounds of 5 min followed by incubation in secondary antibody (goat anti-rat Alexa Fluor 555, 1:500, and donkey anti-rabbit Alexa Fluor 488; Invitrogen) prepared in Antibody Dilution Buffer for 2 h at room temperature in the dark. Sections were rinsed in 1× PBS/0.05% Tween for three rounds of 5 min and incubated in DAPI (D1306: 1:10,000 from 5 mg/ml stock; Invitrogen Molecular Probes) for 10 min. Sections were rinsed in 1× PBS/0.05% Tween for two rounds of 5 min and either removed from the Sequenza Clips and quickly rinsed in 1× PBS or directly mounted onto Fisherbrand Superfrost Plus microscope slides for free-floating sections. Sections were then coverslipped with Invitrogen Prolong Glass Antifade Mountant and cured overnight at room temperature.

Image acquisition and quantification of CNS parenchymal antibody levels
Images of whole slide-mounted immunostained sagittal mouse brain sections were acquired using a wide-field epifluorescence slide scanning microscope (Axio Scan Z1; Carl Zeiss), with a 40×/0.95-NA air objective and filter sets to specifically image Alexa Fluor 488–, 555–, and 647–labeled secondary antibodies.

Exposure times were held constant for each channel across all fields, sections, and slides imaged. Every field for each tissue section was collected, and uniform shading correction and post-stitching was performed with Zeiss Zen Blue Edition software (v3.1). To quantify levels of huIgG present in the brain parenchyma of test subject animals, collected images were quantified using Zen software. Specifically, a custom macro script was written to identify blood vessels present in the tissue, based on morphology and high levels of huIgG signal observed in the vessels of injected animals. Vessels were masked out of subsequent image analyses, leaving only the surrounding parenchymal tissue to be quantified. Specific subregions of the brain sections were selected for quantification (cortex, hippocampus, cerebellum, and hindbrain); positionally similar brain regions were selected across all quantified brain sections. Mean fluorescence intensities corresponding to detected test antibodies in selected brain parenchymal regions were calculated based on the total sum intensity of all parenchymal (non-vessel) pixels in the selected regions divided by the total parenchymal area of the selected region. The ratio of normalized huIgG signal in the brain parenchyma to brain vasculature was quantified as follows:

$$= \frac{\dfrac{\text{Total sum intensity of all parenchymal (non-vessel) pixels in the selected region}}{\text{Total parenchymal area of the selected region}}}{\dfrac{\text{Total sum intensity of all vessel (non-parenchymal) pixels in the selected region}}{\text{Total vessel area of the selected region}}}$$

SRCM and quantification of intracellular antibody levels
To quantify the intracellular localization of huIgG, sections were imaged using a scanning confocal microscope (Leica SP8; Leica Microsystems) operated in superresolution Lightning mode, acquired with a 63×/1.4-NA oil objective at a pixel size of 50 nm and processed using the Adaptive processing algorithm. Confocal z-stacks of 25–30 μm were acquired for each channel using sequential scan settings from three independent cortical brain regions and from three animals in each treatment group. The huIgG signal within the intraneuronal compartment was masked using an intensity-based segmentation of NeuN-positive pixels, and the resulting sum intensities were normalized to the total neuronal volume within a given 3D image field. Intralysosomal huIgG was masked using an intensity-based segmentation of LAMP2-positive pixels, and the huIgG sum intensities were quantified and normalized to the total lysosomal volume. In each case, the mean sum intensity was determined for each animal, and the three means were then used to calculate the mean ± SEM for each treatment.

Tissue or fluid processing for GAG analysis
Tissue (50 mg) was homogenized in 750 μl water using the Qiagen TissueLyzer II for 3 min at 30 Hz. Homogenate was transferred to a 96-well deep plate and sonicated using a 96-tip

Arguello et al.
Architecture determines brain delivery of enzymes

Journal of Experimental Medicine   12 of 15
https://doi.org/10.1084/jem.20211057

sonicator (Q Sonica) for 10 1-s pulses. Sonicated homogenates were spun at 2,500 g for 30 min at 4°C. The resulting lysate was transferred to a clean 96-well deep plate, and a BCA was performed to quantify total protein. 10 µg total protein lysate or 3 µl of CSF was used for subsequent heparin sulfate (HS)/dermatan sulfate (DS) digestion. Digestion was carried out in a PCR plate in a total volume of 62 µl. Internal standard mix of HS and DS (20 ng total) were added to each sample and mixed with Heparinases I, II, and III and chondriotinase B in digestion buffer for 3 h with shaking at 30°C. After digestion, EDTA was added to each sample, and the mixture was boiled at 95°C for 10 min. The digested samples were spun at 3,364 g for 5 min, and samples were transferred to a cellulose acetate filter plate (MSUN03010; Millipore) and spun at 3,364 g for 5 min. The resulting flowthrough was mixed with equal parts of acetonitrile in glass vials and analyzed by mass spectrometry as described below.

Mass spectrometry analysis of GAGs
Quantification of GAG levels in fluids and tissues was performed by liquid chromatography (Nexera X2 system; Shimadzu Scientific Instrument) coupled to electrospray mass spectrometry (6500+ QTRAP; Sciex). For each analysis, sample was injected on a Acquity UPLC BEH Amide 1.7 mm, 2.1 × 150-mm column (Waters Corp.) using a flow rate of 0.6 ml/min with a column temperature of 55°C. Mobile phases A and B consisted of water with 10 mM ammonium formate and 0.1% formic acid (A) and acetonitrile with 0.1% formic acid (B). An isocratic elution was performed with 80% B throughout the 8-min run. Electrospray ionization was performed in the negative-ion mode applying the following settings: curtain gas, 20; collision gas, medium; ion spray voltage, −4,500; temperature, 450°C; ion source, Gas 1, 50; and ion source, Gas 2, 60. Data acquisition was performed using Analyst v1.6.3 or higher (Sciex) in multiple reaction monitoring (MRM) mode, with dwell time (milliseconds) for each species: collision energy, −30; declustering potential, −80; entrance potential, −10; and collision cell exit potential, −10. GAGs were detected as $[M-H]^-$ using the following MRM transitions: D0A0 at m/z 378.1 > 87.0; D0S0 at m/z 416.1 > 138.0; and D0a4 at m/z 458.1 > 300.0. D4UA-2S-GlcNCOEt-6S (HD009; Iduron) at m/z 472.0 (in source fragment ion) > 97.0 was used as internal standard. Individual disaccharide species were identified based on their retention times and MRM transitions using commercially available reference standards (Iduron). GAGs were quantified by the peak area ratio of D0A0, D0S0, and D0a4 to the internal standard using Analyst v1.7.1 or MultiQuant v3.0.2 (Sciex). Reported GAG amounts were normalized to total protein levels as measured by a BCA assay (Pierce). Fold over TfR$^{mu/hu}$ KI values were calculated as follows:

$$= \frac{\text{Average GAG levels of each group}}{\text{Average GAG levels of TfRKI vehicle treated group}}.$$

Percentage reduction from vehicle-treated Ids KO;TfR$^{mu/hu}$ KI mice was calculated as follows:

$$= 100 \times \frac{\left(\begin{array}{l}\text{Average GAG levels of } Ids \text{ KO; TfRKI vehicle treated} \\ \text{group} - \text{Average GAG levels for each treatment group}\end{array}\right)}{\begin{array}{c}\text{Average GAG levels of } Ids \text{ KO; TfRKI} \\ \text{vehicle treated group}\end{array}}$$

HS and DS calibration curves
Pure standards for D0a4 (DS/chondroitin sulfate), D0A0 (HS), and D0S0 (HS) were dissolved in acetonitrile:water 50/50 (vol/vol) to generate a 1-mg/ml stock. An 8-point dilution curve in PBS was generated ranging from 0.12 to 1,000 ng. Subsequently, the internal standard D4UA-2S-GlcNCOEt-6S (20 ng) was added to each serial dilution. Samples were then boiled for 10 min at 95°C and spun at 3,364 g to pellet any particulate matter. Supernatant was filtered using a 30-kD MWCO cellulose acetate filter plate (MSUN03010; Millipore) by spinning at 3,364 g for 5 min at room temperature. Resulting flowthrough was mixed with an equal part of acetonitrile in glass vials and run by mass spectrometry as described above.

Online supplemental material
Fig. S1 shows the binding characterization of IgG:IDS, ETV:IDS, and the polyclonal anti-huIgG reagent used for IHC analysis. Fig. S2 A is a schematic showing the approximate location of sagittal brain regions of interest used for images and quantification in Figs. 4 and S2. Fig. S2, B–D, shows the distribution of ETV:IDS and IgG:IDS into the brain parenchyma across multiple brain regions including the hindbrain, hippocampus, and cerebellum. Fig. S2, E–J, shows the quantification of huIgG staining in the parenchyma and the ratio of normalized huIgG signal in the brain parenchyma to brain vasculature across multiple brain regions. Table S1 provides the PK parameters for Fig. 2. Table S2 provides the GAG values calculated as fold over TfR$^{mu/hu}$ KI and percentage reduction from vehicle-treated Ids KO;TfR$^{mu/hu}$ KI for Fig. 5.

References

Abbott, N.J., M.E. Pizzo, J.E. Preston, D. Janigro, and R.G. Thorne. 2018. The role of brain barriers in fluid movement in the CNS: is there a 'glymphatic' system? *Acta Neuropathol.* 135:387–407. https://doi.org/10.1007/s00401-018-1812-4

Atwal, J.K., Y. Chen, C. Chiu, D.L. Mortensen, W.J. Meilandt, Y. Liu, C.E. Heise, K. Hoyte, W. Luk, Y. Lu, K. Peng, et al. 2011. A therapeutic antibody targeting BACE1 inhibits amyloid-beta production in vivo. *Sci. Transl. Med.* 3:84ra43. https://doi.org/10.1126/scitranslmed.3002254

Banks, W.A. 2016. From blood-brain barrier to blood-brain interface: new opportunities for CNS drug delivery. *Nat. Rev. Drug Discov.* 15:275–292. https://doi.org/10.1038/nrd.2015.21

Bellettato, C.M., and M. Scarpa. 2010. Pathophysiology of neuropathic lysosomal storage disorders. *J. Inherit. Metab. Dis.* 33:347–362. https://doi.org/10.1007/s10545-010-9075-9

Bickel, U., Y.-S. Kang, T. Yoshikawa, and W.M. Pardridge. 1994. In vivo demonstration of subcellular localization of anti-transferrin receptor monoclonal antibody-colloidal gold conjugate in brain capillary endothelium. *J. Histochem. Cytochem.* 42:1493–1497. https://doi.org/10.1177/42.11.7930531

Bien-Ly, N., Y.J. Yu, D. Bumbaca, J. Elstrott, C.A. Boswell, Y. Zhang, W. Luk, Y. Lu, M.S. Dennis, R.M. Weimer, I. Chung, et al. 2014. Transferrin receptor (TfR) trafficking determines brain uptake of TfR antibody affinity variants. *J. Exp. Med.* 211:233–244. https://doi.org/10.1084/jem.20131660

Boado, R.J., J.Z. Lu, E.K. Hui, and W.M. Pardridge. 2018. Reduction in brain heparan sulfate with systemic administration of an IgG Trojan horse-sulfamidase fusion protein in the mucopolysaccharidosis type IIIA mouse. *Mol. Pharm.* 15:602–608. https://doi.org/10.1021/acs.molpharmaceut.7b00958

Demydchuk, M., C.H. Hill, A. Zhou, G. Bunkoczi, P.E. Stein, D. Marchesan, J.E. Deane, and R.J. Read. 2017. Insights into Hunter syndrome from the structure of iduronate-2-sulfatase. *Nat. Commun.* 8:15786. https://doi.org/10.1038/ncomms15786

Dennis, M.S., and R.J. Watts. 2012. Transferrin antibodies into the brain. *Neuropsychopharmacology.* 37:302–303. https://doi.org/10.1038/npp.2011.196

Desnick, R.J., and E.H. Schuchman. 2012. Enzyme replacement therapy for lysosomal diseases: lessons from 20 years of experience and remaining challenges. *Annu. Rev. Genomics Hum. Genet.* 13:307–335. https://doi.org/10.1146/annurev-genom-090711-163739

El-Shewy, H.M., and L.M. Luttrell. 2009. Insulin-like growth factor-2/mannose-6 phosphate receptors. *Vitam. Horm.* 80:667–697. https://doi.org/10.1016/S0083-6729(08)00624-9

Friden, P.M., L.R. Walus, G.F. Musso, M.A. Taylor, B. Malfroy, and R.M. Starzyk. 1991. Anti-transferrin receptor antibody and antibody-drug conjugates cross the blood-brain barrier. *Proc. Natl. Acad. Sci. USA.* 88:4771–4775. https://doi.org/10.1073/pnas.88.11.4771

Haqqani, A.S., G. Thom, M. Burrell, C.E. Delaney, E. Brunette, E. Baumann, C. Sodja, A. Jezierski, C. Webster, and D.B. Stanimirovic. 2018. Intracellular sorting and transcytosis of the rat transferrin receptor antibody OX26 across the blood-brain barrier in vitro is dependent on its binding affinity. *J. Neurochem.* 146:735–752. https://doi.org/10.1111/jnc.14482

Hopkins, C.R., K. Miller, and J.M. Beardmore. 1985. Receptor-mediated endocytosis of transferrin and epidermal growth factor receptors: a comparison of constitutive and ligand-induced uptake. *J. Cell Sci. Suppl.* 3:173–186. https://doi.org/10.1242/jcs.1985.supplement_3.17

Hultqvist, G., S. Syvanen, X.T. Fang, L. Lannfelt, and D. Sehlin. 2017. Bivalent brain shuttle increases antibody uptake by monovalent binding to the transferrin receptor. *Theranostics.* 7:308–318. https://doi.org/10.7150/thno.17155

Jefferies, W.A., M.R. Brandon, S.V. Hunt, A.F. Williams, K.C. Gatter, and D.Y. Mason. 1984. Transferrin receptor on endothelium of brain capillaries. *Nature.* 312:162–163. https://doi.org/10.1038/312162a0

Johnsen, K.B., A. Burkhart, F. Melander, P.J. Kempen, J.B. Vejlebo, P. Siupka, M.S. Nielsen, T.L. Andresen, and T. Moos. 2017. Targeting transferrin receptors at the blood-brain barrier improves the uptake of immunoliposomes and subsequent cargo transport into the brain parenchyma. *Sci. Rep.* 7:10396. https://doi.org/10.1038/s41598-017-11220-1

Johnsen, K.B., A. Burkhart, L.B. Thomsen, T.L. Andresen, and T. Moos. 2019. Targeting the transferrin receptor for brain drug delivery. *Prog. Neurobiol.* 181:101665. https://doi.org/10.1016/j.pneurobio.2019.101665

Jones, A.R., and E.V. Shusta. 2007. Blood-brain barrier transport of therapeutics via receptor-mediation. *Pharm. Res.* 24:1759–1771. https://doi.org/10.1007/s11095-007-9379-0

Kariolis, M.S., R.C. Wells, J.A. Getz, W. Kwan, C.S. Mahon, R. Tong, D.J. Kim, A. Srivastava, C. Bedard, K.R. Henne, T. Giese, et al. 2020. Brain delivery of therapeutic proteins using an Fc fragment blood-brain barrier transport vehicle in mice and monkeys. *Sci. Transl. Med.* 12:eaay1359. https://doi.org/10.1126/scitranslmed.aay1359

Kuang, Y., X. Jiang, Y. Zhang, Y. Lu, H. Ma, Y. Guo, Y. Zhang, S. An, J. Li, L. Liu, Y. Wu, et al. 2016. Dual functional peptide-driven nanoparticles for highly efficient glioma-targeting and drug codelivery. *Mol. Pharm.* 13:1599–1607. https://doi.org/10.1021/acs.molpharmaceut.6b00051

Kumar, N.N., M.E. Pizzo, G. Nehra, B. Wilken-Resman, S. Boroumand, and R.G. Thorne. 2018. Passive immunotherapies for central nervous system disorders: current delivery challenges and new approaches. *Bioconjug. Chem.* 29:3937–3966. https://doi.org/10.1021/acs.bioconjchem.8b00548

Lajoie, J.M., and E.V. Shusta. 2015. Targeting receptor-mediated transport for delivery of biologics across the blood-brain barrier. *Annu. Rev. Pharmacol. Toxicol.* 55:613–631. https://doi.org/10.1146/annurev-pharmtox-010814-124852

Lein, E.S., M.J. Hawrylycz, N. Ao, M. Ayres, A. Bensinger, A. Bernard, A.F. Boe, M.S. Boguski, K.S. Brockway, E.J. Byrnes, L. Chen, et al. 2007. Genome-wide atlas of gene expression in the adult mouse brain. *Nature.* 445:168–176. https://doi.org/10.1038/nature05453

Lesley, J., R. Schulte, and J. Woods. 1989. Modulation of transferrin receptor expression and function by anti-transferrin receptor antibodies and antibody fragments. *Exp. Cell Res.* 182:215–233. https://doi.org/10.1016/0014-4827(89)90293-0

Lu, J.Z., E.K. Hui, R.J. Boado, and W.M. Pardridge. 2010. Genetic engineering of a bifunctional IgG fusion protein with iduronate-2-sulfatase. *Bioconjug. Chem.* 21:151–156. https://doi.org/10.1021/bc900382q

Manich, G., I. Cabezon, J. del Valle, J. Duran-Vilaregut, A. Camins, M. Pallas, C. Pelegri, and J. Vilaplana. 2013. Study of the transcytosis of an anti-transferrin receptor antibody with a Fab' cargo across the blood-brain barrier in mice. *Eur. J. Pharm. Sci.* 49:556–564. https://doi.org/10.1016/j.ejps.2013.05.027

Millat, G., R. Froissart, I. Maire, and D. Bozon. 1997. Characterization of iduronate sulphatase mutants affecting N-glycosylation sites and the cysteine-84 residue. *Biochem. J.* 326:243–247. https://doi.org/10.1042/bj3260243

Moos, T., and E.H. Morgan. 1998. Evidence for low molecular weight, non-transferrin-bound iron in rat brain and cerebrospinal fluid. *J. Neurosci. Res.* 54:486–494. https://doi.org/10.1002/(SICI)1097-4547(19981115)54:4<486::AID-JNR6>3.0.CO;2-I

Moos, T., and E.H. Morgan. 2001. Restricted transport of anti-transferrin receptor antibody (OX26) through the blood-brain barrier in the rat. *J. Neurochem.* 79:119–129. https://doi.org/10.1046/j.1471-4159.2001.00541.x

Muenzer, J., J.C. Lamsa, A. Garcia, J. Dacosta, J. Garcia, and D.A. Treco. 2002. Enzyme replacement therapy in mucopolysaccharidosis type II (Hunter syndrome): a preliminary report. *Acta Paediatr. Suppl.* 91:98–99. https://doi.org/10.1111/j.1651-2227.2002.tb03115.x

Muenzer, J., J.E. Wraith, M. Beck, R. Giugliani, P. Harmatz, C.M. Eng, A. Vellodi, R. Martin, U. Ramaswami, M. Gucsavas-Calikoglu, S. Vijayaraghavan, et al. 2006. A phase II/III clinical study of enzyme replacement therapy with idursulfase in mucopolysaccharidosis II (Hunter syndrome). *Genet. Med.* 8:465–473. https://doi.org/10.1097/01.gim.0000232477.37660.fb

Muldoon, L.L., J.I. Alvarez, D.J. Begley, R.J. Boado, G.J. Del Zoppo, N.D. Doolittle, B. Engelhardt, J.M. Hallenbeck, R.R. Lonser, J.R. Ohlfest, A. Prat,

et al. 2013. Immunologic privilege in the central nervous system and the blood-brain barrier. *J. Cereb. Blood Flow Metab.* 33:13–21. https://doi.org/10.1038/jcbfm.2012.153

NCT04251026. 2022.A study of DNL310 in pediatric subjects with Hunter syndrome. https://ClinicalTrials.gov/show/NCT04251026

Neufeld, E.F. 1991. Lysosomal storage diseases. *Annu. Rev. Biochem.* 60:257–280. https://doi.org/10.1146/annurev.bi.60.070191.001353

Niewoehner, J., B. Bohrmann, L. Collin, E. Urich, H. Sade, P. Maier, P. Rueger, J.O. Stracke, W. Lau, A.C. Tissot, H. Loetscher, et al. 2014. Increased brain penetration and potency of a therapeutic antibody using a monovalent molecular shuttle. *Neuron.* 81:49–60. https://doi.org/10.1016/j.neuron.2013.10.061

Noh, H., and J.I. Lee. 2014. Current and potential therapeutic strategies for mucopolysaccharidoses. *J. Clin. Pharm. Ther.* 39:215–224. https://doi.org/10.1111/jcpt.12136

Okuyama, T., Y. Eto, N. Sakai, K. Minami, T. Yamamoto, H. Sonoda, M. Yamaoka, K. Tachibana, T. Hirato, and Y. Sato. 2019. Iduronate-2-Sulfatase with anti-human transferrin receptor antibody for neuropathic mucopolysaccharidosis II: a phase 1/2 trial. *Mol. Ther.* 27:456–464. https://doi.org/10.1016/j.ymthe.2018.12.005.

Okuyama, T., Y. Eto, N. Sakai, K. Nakamura, T. Yamamoto, M. Yamaoka, T. Ikeda, S. So, K. Tanizawa, H. Sonoda, and Y. Sato. 2021. A phase 2/3 trial of pabinafusp alfa, IDS fused with anti-human transferrin receptor antibody, targeting neurodegeneration in MPS-II. *Mol. Ther.* 29:671–679. https://doi.org/10.1016/j.ymthe.2020.09.039

Pardridge, W.M. 2015. Blood-brain barrier drug delivery of IgG fusion proteins with a transferrin receptor monoclonal antibody. *Expert Opin. Drug Deliv.* 12:207–222. https://doi.org/10.1517/17425247.2014.952627

Parenti, G., G. Andria, and K.J. Valenzano. 2015. Pharmacological chaperone therapy: preclinical development, clinical translation, and prospects for the treatment of lysosomal storage disorders. *Mol. Ther.* 23:1138–1148. https://doi.org/10.1038/mt.2015.62

Parini, R., and F. Deodato. 2020. Intravenous enzyme replacement therapy in mucopolysaccharidoses: clinical effectiveness and limitations. *Int. J. Mol. Sci.* 21:2975. https://doi.org/10.3390/ijms21082975

Paris-Robidas, S., V. Emond, C. Tremblay, D. Soulet, and F. Calon. 2011. In vivo labeling of brain capillary endothelial cells after intravenous injection of monoclonal antibodies targeting the transferrin receptor. *Mol. Pharmacol.* 80:32–39. https://doi.org/10.1124/mol.111.071027

Paterson, J., and C.I. Webster. 2016. Exploiting transferrin receptor for delivering drugs across the blood-brain barrier. *Drug Discov. Today Technol.* 20:49–52. https://doi.org/10.1016/j.ddtec.2016.07.009

Platt, F.M., B. Boland, and A.C. van der Spoel. 2012. The cell biology of disease: lysosomal storage disorders: the cellular impact of lysosomal dysfunction. *J. Cell Biol.* 199:723–734. https://doi.org/10.1083/jcb.201208152

Poduslo, J.F., G.L. Curran, and C.T. Berg. 1994. Macromolecular permeability across the blood-nerve and blood-brain barriers. *Proc. Natl. Acad. Sci. USA.* 91:5705–5709. https://doi.org/10.1073/pnas.91.12.5705

Preston, J.E., N. Joan Abbott, and D.J. Begley. 2014. Transcytosis of macromolecules at the blood-brain barrier. *Adv. Pharmacol.* 71:147–163. https://doi.org/10.1016/bs.apha.2014.06.001

Profaci, C.P., R.N. Munji, R.S. Pulido, and R. Daneman. 2020. The blood-brain barrier in health and disease: important unanswered questions. *J. Exp. Med.* 217:e20190062. https://doi.org/10.1084/jem.20190062

Scarpa, M., C.M. Bellettato, C. Lampe, and D.J. Begley. 2015. Neuronopathic lysosomal storage disorders: approaches to treat the central nervous system. *Best Pract. Res. Clin. Endocrinol. Metab.* 29:159–171. https://doi.org/10.1016/j.beem.2014.12.001

Scarpa, M., P.J. Orchard, A. Schulz, P.I. Dickson, M.E. Haskins, M.L. Escolar, and R. Giugliani. 2017. Treatment of brain disease in the mucopolysaccharidoses. *Mol. Genet. Metab.* 122S:25–34. https://doi.org/10.1016/j.ymgme.2017.10.007

Schultz, M.L., L. Tecedor, M. Chang, and B.L. Davidson. 2011. Clarifying lysosomal storage diseases. *Trends Neurosci.* 34:401–410. https://doi.org/10.1016/j.tins.2011.05.006

Sohn, Y.B., S.Y. Cho, S.W. Park, S.J. Kim, A.R. Ko, E.K. Kwon, S.J. Han, and D.K. Jin. 2013. Phase I/II clinical trial of enzyme replacement therapy with idursulfase beta in patients with mucopolysaccharidosis II (Hunter syndrome). *Orphanet J. Rare Dis.* 8:42. https://doi.org/10.1186/1750-1172-8-42

Sonoda, H., H. Morimoto, E. Yoden, Y. Koshimura, M. Kinoshita, G. Golovina, H. Takagi, R. Yamamoto, K. Minami, A. Mizoguchi, K. Tachibana, et al. 2018. A blood-brain-barrier-penetrating anti-human transferrin receptor antibody fusion protein for neuronopathic mucopolysaccharidosis II. *Mol. Ther.* 26:1366–1374. https://doi.org/10.1016/j.ymthe.2018.02.032

St-Amour, I., I. Pare, W. Alata, K. Coulombe, C. Ringuette-Goulet, J. Drouin-Ouellet, M. Vandal, D. Soulet, R. Bazin, and F. Calon. 2013. Brain bioavailability of human intravenous immunoglobulin and its transport through the murine blood-brain barrier. *J. Cereb. Blood Flow Metab.* 33:1983–1992. https://doi.org/10.1038/jcbfm.2013.160

Stanimirovic, D.B., J.K. Sandhu, and W.J. Costain. 2018. Emerging technologies for delivery of biotherapeutics and gene therapy across the blood-brain barrier. *BioDrugs.* 32:547–559. https://doi.org/10.1007/s40259-018-0309-y

Terstappen, G.C., A.H. Meyer, R.D. Bell, and W. Zhang. 2021. Strategies for delivering therapeutics across the blood-brain barrier. *Nat. Rev. Drug Discov.* 20:362–383. https://doi.org/10.1038/s41573-021-00139-y

Triguero, D., J. Buciak, and W.M. Pardridge. 1990. Capillary depletion method for quantification of blood-brain barrier transport of circulating peptides and plasma proteins. *J. Neurochem.* 54:1882–1888. https://doi.org/10.1111/j.1471-4159.1990.tb04886.x

Ullman, J.C., A. Arguello, J.A. Getz, A. Bhalla, C.S. Mahon, J. Wang, T. Giese, C. Bedard, D.J. Kim, J.R. Blumenfeld, N. Liang, et al. 2020. Brain delivery and activity of a lysosomal enzyme using a blood-brain barrier transport vehicle in mice. *Sci. Transl. Med.* 12:eaay1163. https://doi.org/10.1126/scitranslmed.aay1163

Urayama, A. 2013. Toward the successful delivery of lysosomal enzymes across the blood–brain barrier. *Clin. Exp. Neuroimmunol.* 4:228–238. https://doi.org/10.1111/cen3.12037

Urayama, A., J.H. Grubb, W.S. Sly, and W.A. Banks. 2004. Developmentally regulated mannose 6-phosphate receptor-mediated transport of a lysosomal enzyme across the blood-brain barrier. *Proc. Natl. Acad. Sci. USA.* 101:12658–12663. https://doi.org/10.1073/pnas.0405042101

Urayama, A., J.H. Grubb, W.S. Sly, and W.A. Banks. 2008. Mannose 6-phosphate receptor-mediated transport of sulfamidase across the blood-brain barrier in the newborn mouse. *Mol. Ther.* 16:1261–1266. https://doi.org/10.1038/mt.2008.84

Villasenor, R., J. Lampe, M. Schwaninger, and L. Collin. 2019. Intracellular transport and regulation of transcytosis across the blood-brain barrier. *Cell. Mol. Life Sci.* 76:1081–1092. https://doi.org/10.1007/s00018-018-2982-x

Villasenor, R., M. Schilling, J. Sundaresan, Y. Lutz, and L. Collin. 2017. Sorting tubules regulate blood-brain barrier transcytosis. *Cell Rep.* 21:3256–3270. https://doi.org/10.1016/j.celrep.2017.11.055

Voznyi, Y.V., J.L. Keulemans, and O.P. van Diggelen. 2001. A fluorimetric enzyme assay for the diagnosis of MPS II (Hunter disease). *J. Inherit. Metab. Dis.* 24:675–680. https://doi.org/10.1023/a:1012763026526

Weber, F., B. Bohrmann, J. Niewoehner, J.A.A. Fischer, P. Rueger, G. Tiefenthaler, J. Moelleken, A. Bujotzek, K. Brady, T. Singer, M. Ebeling, et al. 2018. Brain shuttle antibody for Alzheimer's disease with attenuated peripheral effector function due to an inverted binding mode. *Cell Rep.* 22:149–162. https://doi.org/10.1016/j.celrep.2017.12.019

Webster, C.I., J. Hatcher, M. Burrell, G. Thom, P. Thornton, I. Gurrell, and I. Chessell. 2017. Enhanced delivery of IL-1 receptor antagonist to the central nervous system as a novel anti-transferrin receptor-IL-1RA fusion reverses neuropathic mechanical hypersensitivity. *Pain.* 158:660–668. https://doi.org/10.1097/j.pain.0000000000000810

Weflen, A.W., N. Baier, Q.J. Tang, M. Van den Hof, R.S. Blumberg, W.I. Lencer, and R.H. Massol. 2013. Multivalent immune complexes divert FcRn to lysosomes by exclusion from recycling sorting tubules. *Mol. Biol. Cell.* 24:2398–2405. https://doi.org/10.1091/mbc.E13-04-0174

Wolak, D.J., M.E. Pizzo, and R.G. Thorne. 2015. Probing the extracellular diffusion of antibodies in brain using in vivo integrative optical imaging and ex vivo fluorescence imaging. *J. Control. Release.* 197:78–86. https://doi.org/10.1016/j.jconrel.2014.10.034

Wolak, D.J., and R.G. Thorne. 2013. Diffusion of macromolecules in the brain: implications for drug delivery. *Mol. Pharm.* 10:1492–1504. https://doi.org/10.1021/mp300495e

Wraith, J.E., M. Scarpa, M. Beck, O.A. Bodamer, L. De Meirleir, N. Guffon, A. Meldgaard Lund, G. Malm, A.T. Van der Ploeg, and J. Zeman. 2008. Mucopolysaccharidosis type II (Hunter syndrome): a clinical review and recommendations for treatment in the era of enzyme replacement therapy. *Eur. J. Pediatr.* 167:267–277. https://doi.org/10.1007/s00431-007-0635-4

Yu, Y.J., Y. Zhang, M. Kenrick, K. Hoyte, W. Luk, Y. Lu, J. Atwal, J.M. Elliott, S. Prabhu, R.J. Watts, and M.S. Dennis. 2011. Boosting brain uptake of a therapeutic antibody by reducing its affinity for a transcytosis target. *Sci. Transl. Med.* 3:84ra44. https://doi.org/10.1126/scitranslmed.3002230

Zhou, Q.H., R.J. Boado, J.Z. Lu, E.K. Hui, and W.M. Pardridge. 2012. Brain-penetrating IgG-iduronate 2-sulfatase fusion protein for the mouse. *Drug Metab. Dispos.* 40:329–335. https://doi.org/10.1124/dmd.111.042903
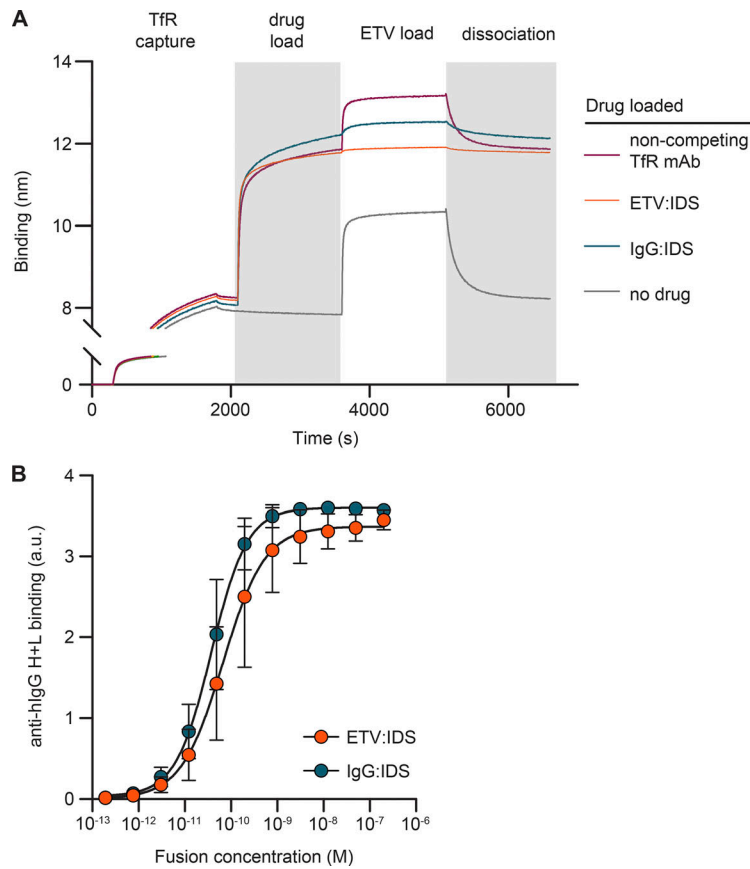
Supplemental material

Figure S1. **Binding characterization of IgG:IDS, ETV:IDS, and the polyclonal anti-huIgG reagent used for IHC. (A)** Competition binding of ETV:IDS and IgG:IDS as measured by biolayer interferometry. Full-length human TfR-loaded biosensors were used to capture ETV:IDS, IgG:IDS, or an anti-TfR antibody known not to compete with ETV:IDS. The ability to subsequently bind to ETV:IDS was tested, demonstrating that both ETV:IDS and IgG:IDS compete for TfR binding. **(B)** Binding of ETV:IDS and IgG:IDS to the anti–human IgG H+L polyclonal antibody used in IHC experiments was determined by ELISA; data presented represent the average of three technical replicates, with n = 3 per replicate. a.u., arbitrary unit.
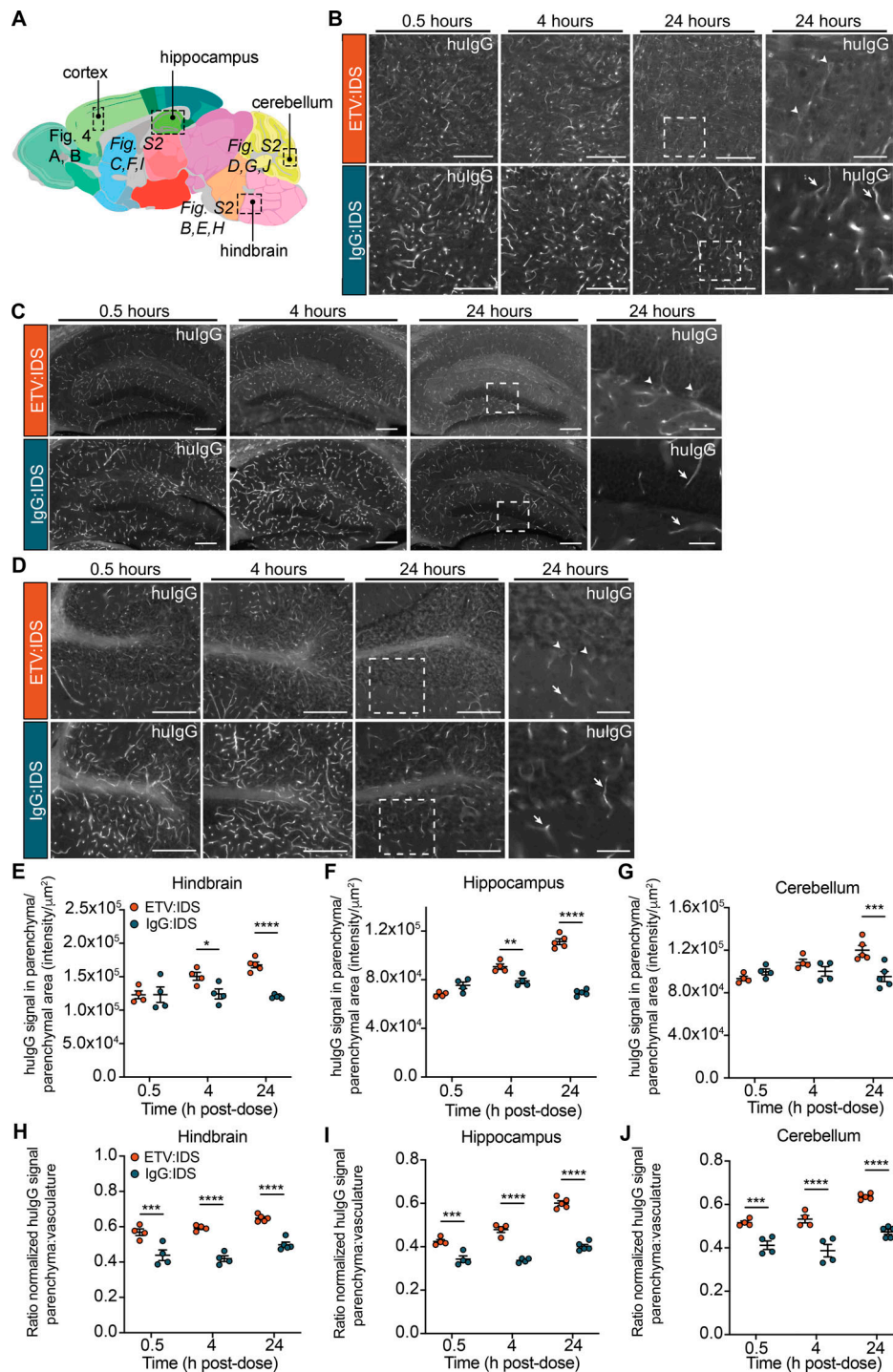
Figure S2. IHC localization of ETV:IDS demonstrates more effective distribution into the brain parenchyma than IgG:IDS across multiple brain regions. The distribution of ETV:IDS and IgG:IDS was assessed using sagittal brain sections from TfR$^{mu/hu}$ KI mice 0.5, 4, and 24 h after an IV dose of 10 mg/kg. TfR$^{mu/hu}$ KI mice are on a C57BL/6 background. **(A)** Schematic indicating approximate location of sagittal brain regions of interest (ROIs) for images and quantification in Fig. 4, A and B (cortex), and Fig. S2 (hindbrain, hippocampus, and cerebellum; adapted from the *Allen Adult Mouse Brain Atlas*; original image credit: Allen Institute; Lein et al. [2007]). **(B–D)** Sections were immunostained with antibodies against huIgG, imaged, and post-stitched using a wide-field fluorescence slide scanner in the hindbrain (B), hippocampus (C), and cerebellum (D). Scale bars = 200 µm. Dashed boxes indicate regions shown at higher magnification displayed in the far-right panel; scale bars = 50 µm. Arrows indicate huIgG staining localized to vascular profiles; arrowheads indicate cellular internalization of huIgG staining. **(E–G)** Quantification of huIgG staining in the parenchyma of the hindbrain (E), hippocampus (F), and cerebellum (G) was calculated based on the total sum intensity of all parenchymal staining in the ROI divided by the total parenchymal area in the ROI. A custom macro script was used to identify blood vessels present in the tissue and masked out of subsequent image analyses. **(H–J)** The ratio of normalized huIgG signal in the brain parenchyma to brain vasculature was also quantified in the hindbrain (H), hippocampus (I), and cerebellum (J). Data presented are from a single study with n = 4–5 mice per group. Each symbol represents a biological replicate. Graphs display mean ± SEM and P values: two-way ANOVA with Sidak's multiple comparison test; *, $P \leq 0.05$; **, $P \leq 0.01$; ***, $P \leq 0.001$; ****, $P \leq 0.0001$.

Arguello et al.
Architecture determines brain delivery of enzymes

Journal of Experimental Medicine S2
https://doi.org/10.1084/jem.20211057

Provided online are Table S1 and Table S2. Table S1 lists PK parameters. Table S2 shows that ETV:IDS is more effective than IgG:IDS at reducing brain and CSF GAGs in *Ids* KO;TfR$^{mu/hu}$ KI mice.